ADER Discontinuous Galerkin Material Point Method

Alaa Lakiss, Thomas Heuzé, Mikhael Tannous, Laurent Stainier

ADER Discontinuous Galerkin Material Point Method

Alaa Lakiss[a], Thomas Heuzé[a,*], Mikhael Tannous[b], Laurent Stainier[a]

[a]*Research Institute in Civil and Mechanical Engineering GeM, UMR 6183 CNRS, Ecole Centrale de Nantes, 1 rue de la Noë, 44321 Nantes, France*

[b]*Lebanese University, Faculty of Engineering, Tripoli, Lebanon.*

Abstract

The *first-order* accurate Discontinuous Galerkin Material Point Method (DGMPM), initially introduced by Renaud et *al*. [55], considers a solid body discretized by a collection of material points carrying the history of the matter, embedded in an arbitrary grid on which a nodal Discontinuous Galerkin approximation is defined, and that serves to solve balance equations. This method has been shown to be promising, especially for solving hyperbolic problems in finite deforming solids [57, 56]. The main goal of this research is to extend the *first-order* DGMPM to arbitrary high-order accurate approximations. This is performed by adapting the ADER (Arbitrary high order DErivative Riemann problem) approach [15] to the particular spatial discretization of the DGMPM. Firstly, the predictor step permits to design a particle-to-grid projection of arbitrary high order of accuracy, consistent with that of the nodal discontinuous Galerkin approximation defined on the arbitrary grid. This is performed using a Moving Least Square approximation for the ADER predictor field. Secondly, since the degrees of freedom of the predictor field are now defined at material points, the computation of the constitutive response of the material is ensured to be always performed at these material points. This is of crucial importance for history-dependent constitutive models because it avoids any diffusive transfer of internal variables on a new computational grid. Finally, a total Lagrangian formulation of equations is kept, which allows to precompute once and for all both the nodal discontinuous Galerkin approximation and that of the ADER predictor field, until the arbitrary grid is discarded if required. The method is illustrated on a few two-dimensional numerical examples, on which comparisons are shown with the ADER-DGFEM and Runge-Kutta-DGFEM.

Keywords: Discontinuous Galerkin Material Point Method, ADER schemes, Finite deforming hyperelastic solids, ADER-DGMPM, Hyperbolic problems

1. Introduction

High resolution numerical simulations of impacts on dissipative solids aim at reproducing the history of loading undergone by the material points, while freeing from any numerical disturbance that might impair the understanding of physical phenomena of interest. These simulations are of great importance for many engineering applications such as crash-proof design, or high speed forming processes, and mainly consist in solving hyperbolic initial boundary value problems, whose solutions consist of both continuous and discontinuous waves [40]. On the one hand, accurate capturing of both wave fronts and propagation of irreversible phenomena is of primal importance in order to be able to relate the history of wave paths in the medium to its residual fields once the steady state is achieved. On the other hand, the solid medium may undergo large strains, as a consequence of the applied impact.

The construction of numerical approximations of these solutions face two main challenges which may combine with each other during the simulation. The first one is related to the finite deformations which may occur. The Lagrangian or material description is very popular in the solid mechanics community since it allows to accurately track boundaries and particle pathlines, especially for history-dependent constitutive response. But Lagrangian mesh-based approximations are subject to mesh entanglement and may require re-meshing and diffusive projection steps [16, 47].

*Corresponding author

Email address: thomas.heuze@ec-nantes.fr (Thomas Heuzé)

The Eulerian description is free from the mesh tangling issues, but requires interface tracking techniques plus the (diffusive) transport of internal variables [48, 5, 35]. Arbitrary-Lagrangian-Eulerian (ALE) approaches were designed to meet the advantages of the two above descriptions [18], but usually also combine their drawbacks especially for dissipative constitutive responses [7]. Following a Lagrangian description, mesh-free methods aim at freeing the numerical simulation from mesh tangling issues [6, 42, 52]. However, on the one hand these methods have their own problems (prescribing boundary conditions, among others), and on the other hand their approximations were not developed for shock-capturing purpose, and give quite poor results for those problems as shown for instance in [45].

The second challenge is the problem of the approximation of discontinuous solutions, and the development of high order numerical schemes for hyperbolic conservation laws. This challenge has been addressed continously since the 1950s, especially with the introduction of non-linear approximations such as, but not limited to, the Total Variation Disminishing methods (TVD) (see e.g. [63, 30, 41]), the family of ENO and WENO schemes [32, 31, 61], and more recently the ADER approach (Arbitrary high order DErivative Riemann problem) [67, 59, 65], which can either be applied in the contexts of the Finite Volume (FV) Method [20, 11, 12, 13] or the Discontinuous Galerkin Finite Element Method (DGFEM) [54, 22, 15]. Although ADER was first thought as a way to solve a generalized Riemann problem[8] (GRP) coupled to a MUSCL[69] approach [67, 59], it was later reformulated as a local space-time discontinuous Galerkin predictor solved cellwise, whose approximation enabled to solve a set of classical Riemann problems along the time axis at each element interface. Non-oscillatory solutions are then obtained by applying to the ADER solution an *a posteriori* sub-cell WENO-FV-based limiter, based on the MOOD algorithm [21].

Althought the combination of the above two challenges have been addressed successfully with an Eulerian description (see e.g. [51, 64]), the construction of shock-capturing methods able to compute large strains with a Lagrangian description is not a closed problem, and remains a challenge in itself. For instance, the approximations related to some well-known mesh-free methods developed in the 1980s and the 1990s are still the topic of adaption for shock-capturing purpose. To this end, some Lagrangian conservative particle-based methods have been recently developed for problems in solid mechanics involving large strains. One example is the Smooth Particle Hydrodynamics (SPH) method [43, 49], applied for solid mechanics problems with a conservative formulation in the isothermal setting [39], then extended to thermoelasticity[24]. Another example is the Discontinuous Galerkin Material Point Method (DGMPM)[55, 57, 56], which combines the DGFEM [17] with the Material Point Method[62] (MPM). The latter comes from the family of Particle-In-Cell methods (PIC)[28] developed in the 1960s. The solid body is discretized into a set of particles carrying the fields of a problem that move in an arbitrary computational mesh, which is used for the solution of balance equations. In a sense, this double discretization (material points plus a grid) permits to dissociate the motion of material particles from that of the computational mesh, but without any transfer of internal variables and additional convection terms as the grid is discarded as also done in an ALE approach. The DGMPM brought several novelties with respect to the MPM: (i) the set of equations was formulated within a total Lagrangian framework, in order to get rid of the grid-crossing instabilities [2], and (ii) following conservative formulations in order to be compatible with the discontinuous Galerkin approximation defined on the arbitrary grid, interface fluxes being computed from the solution of approximate Riemann solvers.

Despite that the DGMPM has been shown to be promising for solving hyperbolic problems in finite deforming solids with a Lagrangian description, its approximation is only first order-accurate[57]. Its extension to arbitrary high orders of approximation is the purpose of the present work. However, several issues prevent at first this straightforward extension. First, the projection functions from particles to grid inherited from MPM are Shepard's functions[60], whose smoothness is not sufficient to increase the order of accuracy of the method. Second, the computation of integrals of the weak form uses a quadrature based on material points, also inherited from MPM, which is not sufficiently accurate. Third, the crucial point the method should meet to address history-dependent constitutive responses is to ensure that internal variables always lie at material points, in order to avoid diffusive projection steps of the loading history. Explicit Runge-Kutta (RK) methods may not appear as the best suited time integrators to satisfy this last condition. For instance, the second stage of a RK2 requires (see Eq. $(7)_2$ in a previous analysis of DGMPM[57]) the computation of fluxes and hence of stresses at mid-time step at nodes. On the one hand, a projection of internal variables to grid nodes in order to perform a constitutive update would lead to severe numerical diffusion, which cannot be afforded. On the other hand, keeping internal variables at material points for constitutive updates would require as many back and forth transfers of strains or stresses between material points and grid nodes as the number of stages the Runge-Kutta time integrator consists of, which would moreover lead to additional numerical diffusion.

In this paper, the extension of the first-order DGMPM to arbitrary high-order accurate approximations is performed

by adapting the ADER approach to the particular spatial discretization of the DGMPM. Two main novelties are brought with respect to ADER-DGFEM. First, the predictor step permits to design a particle-to-grid projection of arbitrary high order of accuracy, consistent with that of the nodal discontinuous Galerkin approximation defined on the arbitrary grid. This is performed using a Moving Least Square (MLS) approximation[6] for the ADER predictor field. Second, the degrees of freedom of the ADER-predictor fields are now defined at material points, and not at interpolation points as it is the case for ADER-DGFEM. Hence, the contitutive update is ensured to be always performed at these material points. Internal variables are never changed of geometrical support, whether during a time increment or when the arbitrary computational grid is discarded and rebuilt for any purpose. At last, thanks to the total Lagrangian framework of the formulation, both the discontinuous Galerkin approximation and the particle to grid mapping are computed once and for all at the beginning of the computation, until the grid is discarded.

In this paper, the ADER-DGMPM is first presented in the context of Lagrangian isothermal hyperelastodynamics, whose model problem is first recalled in Section 2. Next, the space-time discretization and associated basics of DGFEM (actually the corrector step) are presented in Section 3. The predictor of the ADER-DGMPM is then presented in Section 4, as well as the global solution procedure. Finally, some numerical illustrations are shown in Section 5, especially presenting comparisons with numerical results obtained with RK-DGFEM and ADER-DGFEM.

2. Model continuous problem: Lagrangian isothermal hyperelastodynamics

2.1. Conservation laws

We consider a continuous solid body Ω, of initial configuration $\Omega_0 \in \mathbb{R}^d$, of boundary $\partial\Omega_0$ and outward unit normal $\mathbf{N}$, d is the space dimension. The motion of this body is described by the mapping $\boldsymbol{\phi}(\mathbf{X}, t)$ relating the position of a material point of coordinate $\mathbf{X} \in \Omega_0$ in the initial configuration to its current coordinates $\mathbf{x} \in \Omega(t)$. From this mapping, the rate of the deformation gradient two-point tensor $\dot{\mathbf{F}}$ is the material gradient of the material velocity vector $\mathbf{v}$

$$\dot{\mathbf{F}}(\mathbf{X}, t) = \mathrm{GRAD}\,\mathbf{v} \quad \forall \mathbf{X} \in \Omega_0. \tag{1}$$

Equation (1) can be rewritten as a geometrical conservation law [53, 68, 38]

$$\dot{\mathbf{F}} - \mathrm{DIV}(\mathbf{v} \otimes \mathbf{1}) = 0. \tag{2}$$

The material divergence DIV is computed with respect to initial coordinates $\mathbf{X}$, and $\mathbf{1}$ is the identity of second order. From Equation (1), it is evident that the material CURL of the deformation gradient $\mathbf{F}$ vanishes

$$\mathrm{CURL}\,\mathbf{F} = 0. \tag{3}$$

The conservation of the linear momentum should also be satisfied. Neglecting body forces, it reads in its material form

$$\frac{\partial \mathbf{p}}{\partial t} - \mathrm{DIV}\,\mathbf{P} = 0 \tag{4}$$

where $\mathbf{p} = \rho_0 \mathbf{v}$ denotes the density of linear momentum per unit undeformed volume, $\rho_0(\mathbf{X}) = \rho(\mathbf{X}, t = 0)$ is the reference mass density, $\mathbf{P}$ denotes the first Piola-Kirchhoff stress tensor. Gathering Equations (2) and (4) allows to form the following system of conservation laws

$$\frac{\partial \boldsymbol{\mathcal{U}}}{\partial t} + \mathrm{DIV}\,\boldsymbol{\mathcal{F}} = 0, \tag{5}$$

consisting of M scalar equations, where $\boldsymbol{\mathcal{U}}$ and $\boldsymbol{\mathcal{F}}$ denote the vector of conserved quantities and the flux vector respectively, defined as

$$\boldsymbol{\mathcal{U}} = \begin{Bmatrix} \mathbf{F} \\ \mathbf{p} \end{Bmatrix} \quad ; \quad \boldsymbol{\mathcal{F}} = \begin{Bmatrix} -\mathbf{v} \otimes \mathbf{1} \\ -\mathbf{P} \end{Bmatrix}. \tag{6}$$

System (5) also reads in castesian coordinates as

$$\frac{\partial \boldsymbol{\mathcal{U}}}{\partial t} + \sum_{\alpha=1}^{3} \frac{\partial \boldsymbol{\mathcal{F}}_\alpha}{\partial X_\alpha} = 0, \tag{7}$$

with the flux vector $\boldsymbol{\mathcal{F}}_\alpha = \boldsymbol{\mathcal{F}} \cdot \mathbf{E}_\alpha$ in the α-th material direction $\mathbf{E}_\alpha$, defined as

$$\boldsymbol{\mathcal{F}}_\alpha = \begin{Bmatrix} -\mathbf{v} \otimes \mathbf{E}_\alpha \\ -\mathbf{P} \cdot \mathbf{E}_\alpha \end{Bmatrix}. \tag{8}$$

System (5) reduces to the well-known Rankine-Hugoniot jump conditions across any discontinuity of fields

$$S\,[\boldsymbol{\mathcal{U}}] = [\boldsymbol{\mathcal{F}}] \cdot \mathbf{N}, \tag{9}$$

where $\mathbf{N}$ is the material normal of the discontinuity surface moving at speed S, and $[\bullet]$ denotes the jump of the quantity $(\bullet)$ across the discontinuity, such that $[\bullet] = (\bullet)^+ - (\bullet)^-$.

2.2. Quasi-linear form

It is also convenient to introduce the auxiliary vector $\boldsymbol{Q}$ defined as

$$\boldsymbol{Q} = \begin{Bmatrix} \mathbf{P} \\ \mathbf{v} \end{Bmatrix}, \tag{10}$$

including the stresses $\mathbf{P}$, and satisfying to the following quasi-linear form

$$\frac{\partial \boldsymbol{Q}}{\partial t} + \boldsymbol{\mathcal{A}}_\alpha \frac{\partial \boldsymbol{Q}}{\partial X_\alpha} = 0 \tag{11}$$

obtained from the conservation laws (5)[55], with

$$\boldsymbol{\mathcal{A}}_\alpha = \frac{\partial \boldsymbol{Q}}{\partial \boldsymbol{\mathcal{U}}} \frac{\partial \boldsymbol{\mathcal{F}}_\alpha}{\partial \boldsymbol{Q}} = -\begin{bmatrix} \mathbf{0}_4 & \frac{\partial \mathbf{P}}{\partial \mathbf{F}} \cdot \mathbf{E}_\alpha \\ \frac{\mathbf{1} \otimes \mathbf{E}_\alpha}{\rho_0} & \mathbf{0}_3 \end{bmatrix}, \tag{12}$$

where $\mathbf{0}_k$ denotes the kth-order zero tensor, and the fourth-order tangent moduli tensor $\frac{\partial \mathbf{P}}{\partial \mathbf{F}}$ explicitly appears, which are provided by the chosen constitutive model discussed in the next section.

2.3. Constitutive model

A hyperelastic constitutive modeling is taken as a model response in this work, described by the stored-energy potential $W(\mathbf{F})$ which is a function of the deformation gradient $\mathbf{F}$. More precisely, the elastic energy density W is usually split into volumetric and isochoric parts[10]

$$W(\mathbf{F}) = W^H(J) + \bar{W}(\bar{C}), \tag{13}$$

where the volumetric part $W^H(J)$ depends on the jacobian determinant J, and the isochoric component $\bar{W}(\bar{\mathbf{C}})$ is a function of the isochoric Cauchy-Green strain tensor $\bar{\mathbf{C}}$ defined as

$$\bar{\mathbf{F}} = (J)^{-1/3}\mathbf{F}, \quad \det \bar{\mathbf{F}} = 1 \tag{14}$$

$$\bar{\mathbf{C}} = (\bar{\mathbf{F}})^T \cdot \bar{\mathbf{F}}. \tag{15}$$

According to the particular chosen set of conservation laws (5), the jacobian determinant J may either be computed as the determinant of the deformation gradient (i.e. $J = \det \mathbf{F}$), or updated via the solution of an additional conservation law written on it (see e.g. [33, 25]), especially when quasi-incompressible responses[25] or hydrodynamic equation of state[13] are described.

The simplest expression one can consider for the volumetric part $W^H(J)$ is a quadratic one

$$W^H(J) = \frac{\kappa}{2}(J-1)^2, \tag{16}$$

while the isochoric part of the free energy can be described by a family of rank-one convex stored energies[23, 13]

$$\bar{W}(\bar{I}_1, \bar{I}_2) = \frac{\mu}{4}\left[-2a(\bar{I}_1 - 3) + \frac{(1+a)}{3}(\bar{I}_2 - 9)\right], \tag{17}$$

where a is an adjustable parameter, μ is the elastic shear modulus, and invariants $\bar{I}_1$, $\bar{I}_2$ are defined as

$$\bar{I}_1 = \mathrm{tr}\,\bar{\mathbf{C}}, \quad \bar{I}_2 = \frac{1}{2}\left(\mathrm{tr}\,[\bar{\mathbf{C}}]^2 - \mathrm{tr}\,[\bar{\mathbf{C}}^2]\right). \tag{18}$$

In the range $a \in \left[-1, \frac{1}{2}\right]$, it has been shown[23] that the resulting first order system of equations is hyperbolic. In the particular case where $a = -1$, a more classical neo-Hookean material is obtained, whose distortional free energy reads

$$\bar{W}(\bar{I}_1) = \frac{\mu}{2}(\bar{I}_1 - 3). \tag{19}$$

Polyconvex hyperelastic models (e.g. Mooney-Rivlin) are also used by some authors[25, 9], for which the isochoric elastic free energy $\bar{W}$ becomes a function of the three minors of the elastic deformation. The system of conservation laws (5) is then extended to the other deformation minors, so that the resulting first order system of equations is also shown to be hyperbolic [9].

From the stored energy density (13) and the distortional energy density (19), the first Piola-Kirchhoff stresses are expressed as

$$\mathbf{P} = \frac{\partial W}{\partial \mathbf{F}}, \tag{20}$$

and can be split into hydrostatic and shear contributions

$$\mathbf{P} = \mathbf{P}_H + \mathbf{P}_s, \tag{21}$$

defined as

$$\mathbf{P}_H = p\mathbf{H}, \quad p = \frac{\partial W}{\partial J} = \kappa(J-1) \tag{22}$$

$$\mathbf{P}_s = \mu\mathbf{F} \cdot \frac{\partial \bar{I}_1}{\partial \mathbf{C}}, \tag{23}$$

where p is the hydrostatic pressure, and $\mathbf{H}$ the co-factor of the deformation gradient. The acoustic tensor $\mathbf{A}$ is defined from the fourth-order tangent modulus tensor $\mathbb{C}$ as

$$(\mathbf{C}_{NN})_{ij} = C_{i\alpha j\beta} N_\alpha N_\beta \tag{24}$$

$$(\mathbb{C})_{i\alpha j\beta} = \frac{\partial P_{i\alpha}}{\partial F_{j\beta}} = \frac{\partial^2 W}{\partial F_{j\beta} F_{i\alpha}}, \tag{25}$$

where N_α are the components of an arbitrary material normal vector $\mathbf{N}$. The spectral analysis of the jacobian matrix $\mathcal{A}_N = \mathcal{A}_\alpha N_\alpha$ (see Equation (11)) can be shown to be linked to that of the acoustic tensor $\mathbf{C}_{NN}$, which yields distinct and non-zero elastic celerities and associated eigenvectors, as shown in [55], if the stored energy density (13) satisfies the Legendre-Hadamard ellipticity condition.

3. Space-time discretization on the computational grid

The initial configuration Ω_0 of the continuum body Ω is discretized into a set material points which are embedded within an arbitrary computational grid, made of E non-overlapping grid cells of volume Ω_e. Figure 1 shows a two-dimensional example. Let us now focus on one grid cell Ω_e and on the time increment $t \in [t_n, t_{n+1}]$, $n = 1, \ldots, N_{\Delta t}$. From the vector of conserved quantities $\mathbf{U}_p(t_n)$ and the auxiliary vector $\mathbf{Q}_p(t_n)$ assumed to be known *at each material point* $p = 1, \ldots, N_p$ of initial coordinates $\mathbf{X}_p$ lying in the grid cell e at time t_n, plus eventually associated additional internal variables, the objective is to compute updates of these quantities at time t_{n+1}.

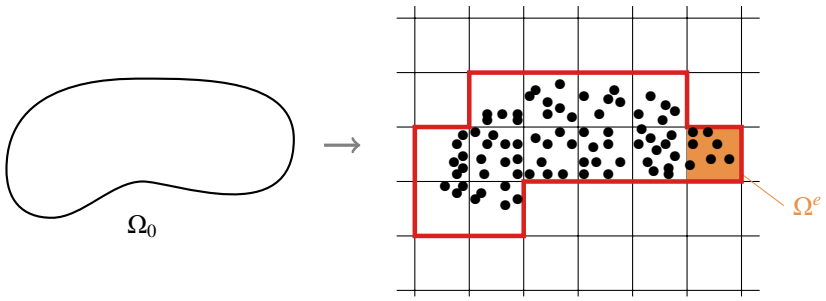

Figure 1: Discretization of the initial configuration Ω_0 of a two-dimensional body Ω using particles in an arbitrary grid.

3.1. Discrete update on the computational grid

The nodal-discontinuous Galerkin framework provides the following approximate solution to that of the system of conservation laws (5) in each grid cell Ω_e:

$$\boldsymbol{\mathcal{U}}_h(\mathbf{X}, t_n)|_{\Omega_e} = \sum_{b=1}^{N_n} \Phi_b(\boldsymbol{\xi}(\mathbf{X}))\hat{\boldsymbol{\mathcal{U}}}_b^n \tag{26}$$

which is *a priori* discontinuous across element boundaries. In the approximation (26), both the degrees of freedom $\hat{\boldsymbol{\mathcal{U}}}_b^n$ defined at time t_n and the shape function $\Phi_b(\boldsymbol{\xi}(\mathbf{X}))$ are associated with the bth spatial interpolation point, which can be of various types (equidistant, Gauss-Legendre or Gauss-Lobatto). More precisely, the shape function $\Phi_b(\boldsymbol{\xi}(\mathbf{X}))$ is a function of parent coordinates $\boldsymbol{\xi}$ which are themselves a function of initial coordinates $\mathbf{X}$ through the inverse geometrical mapping. The shape function $\Phi_b(\boldsymbol{\xi})$ is constructed by a classical tensorisation of one-dimensional Lagrange polynomials on the parent interval. In case of two-dimensional problems, for example considering quadrangular elements, the shape function reads as $\Phi_b(\boldsymbol{\xi}) = \phi_{b_0}(\xi)\phi_{b_1}(\eta)$, b_0 and b_1 being indices related to the first and second directions respectively, and the parent interval may be defined as $\boldsymbol{\xi} = (\xi, \eta) \in [0, 1] \times [0, 1]$.

Multiplying System (5) with the shape function Φ_a, integrating over the space-time domain $\Omega_e \times [t_n, t_{n+1}]$, and integrating by parts with respect to the spatial coordinates X_α gives the following weak form:

$$\int_{t_n}^{t_{n+1}} \int_{\Omega_e} \left(\Phi_a \frac{\partial \boldsymbol{\mathcal{U}}_h}{\partial t} - \frac{\partial \Phi_a}{\partial X_\alpha} \cdot \boldsymbol{\mathcal{F}}_\alpha \right) dV dt + \int_{t_n}^{t_{n+1}} \int_{\Gamma_e} \Phi_a (\boldsymbol{\mathcal{F}} \cdot \mathbf{N}) d\Gamma dt = 0. \tag{27}$$

The introduction of the DG approximation (26) within the weak form (27) gives the following semi-discrete equations

$$\boldsymbol{\mathcal{M}} \left(\hat{\boldsymbol{\mathcal{U}}}_{n+1} - \hat{\boldsymbol{\mathcal{U}}}_n \right) = \int_{t_n}^{t_{n+1}} \boldsymbol{\mathcal{R}}(\boldsymbol{\mathcal{Q}}_h) dt. \tag{28}$$

The mass matrix $\boldsymbol{\mathcal{M}}$ is defined as

$$\boldsymbol{\mathcal{M}} = \left(\int_{\Omega_e} \Phi_a \Phi_b dV \right)_{\substack{1 \le i \le M \\ 1 \le a,b \le N_n}}, \tag{29}$$

hence gathering all nodal shape functions for all scalar equations $i = 1, \ldots, M$. For rectangular grids and normed Legendre polynomials, it becomes the identity matrix[]. However for non-uniform quadrilateral meshes, it is computed with a classical quadrature in the parent domain. The residual fluxes $\boldsymbol{\mathcal{R}}(\boldsymbol{\mathcal{Q}}_h)$ depend on the auxiliary vector $\boldsymbol{\mathcal{Q}}_h$ and are defined as the substraction between the discrete volume and interface fluxes:

$$\boldsymbol{\mathcal{R}}(\boldsymbol{\mathcal{Q}}_h) = \mathbf{F}_v(\boldsymbol{\mathcal{Q}}_h) - \mathbf{F}_s(\boldsymbol{\mathcal{Q}}_h^-, \boldsymbol{\mathcal{Q}}_h^+), \tag{30}$$

where $\boldsymbol{\mathcal{Q}}_h^-, \boldsymbol{\mathcal{Q}}_h^+$ denotes the evaluations of $\boldsymbol{\mathcal{Q}}_h$ on each side of the grid cell interfaces.

The computation of the time integral appearing in Equation (28) with a classical Gauss quadrature permits to compute the sought update on the grid cell

$$\hat{\boldsymbol{\mathcal{U}}}_{n+1} = \hat{\boldsymbol{\mathcal{U}}}_n + \sum_s \omega_s \left[\boldsymbol{\mathcal{M}}^{-1} \boldsymbol{\mathcal{R}} \left(\boldsymbol{\mathcal{Q}}_h(\tau_s), \boldsymbol{\mathcal{Q}}_h^-(\tau_s), \boldsymbol{\mathcal{Q}}_h^+(\tau_s) \right) \right], \tag{31}$$

where ω_s and $\tau_s \in [0,1]$ are the weights and parent coordinates of the time integration points, respectively. The computation of update (31) relies on the ability to provide some evaluations of the auxiliary vector $\boldsymbol{Q}$ at intermediate times τ_s in order to compute the residual fluxes $\boldsymbol{\mathcal{R}}$ at those instants. The ADER approach amounts to replace the Nodal-DG approximation $\boldsymbol{Q}_h$ of the auxiliary vector $\boldsymbol{Q}$ appearing as an argument of the residual fluxes $\boldsymbol{\mathcal{R}}$ by a space-time approximation $\mathbf{q}_h(\mathbf{X}, t)$ of the same vector defined on the control volume $\Omega_e \times [t_n, t_{n+1}]$, called the predictor field, solution of a local auxiliary problem defined in Section 4.1. As a consequence, update (31) is also called the corrector step.

3.2. Computation of fluxes

3.2.1. Volume fluxes

Since the fluxes $\boldsymbol{\mathcal{F}}$ are linear functions of the auxiliary vector $\mathbf{q}$, the discrete volume fluxes can be computed from their pointwise evaluations at interpolation points a as

$$(\mathbf{F}_v)_{ia} = \mathbf{K}_\alpha^{ab} \boldsymbol{\mathcal{F}}_{i\alpha}\left(\mathbf{q}_h(\mathbf{X}_b, \tau_s)\right); \quad \mathbf{K}_\alpha^{ab} = \sum_I \left(w_I \frac{\partial \Phi_a}{\partial \xi_m} \frac{\partial \xi_m}{\partial X_\alpha} \Phi_b \mathcal{J} \right)(\boldsymbol{\xi}_I) \tag{32}$$

where $\boldsymbol{\mathcal{F}}_{i\alpha}$ is the ith component of the fluxes $\boldsymbol{\mathcal{F}}_\alpha = \boldsymbol{\mathcal{F}} \cdot \mathbf{E}_\alpha$, $\mathbf{q}_h(\mathbf{X}_b, \tau_s)$ denotes the space-time approximation of the auxiliary vector evaluated at the bth spatial interpolation point and at intermediate time τ_s, $\mathcal{J}$ and $\partial \xi_m / \partial X_\alpha$ are the jacobian determinant of the geometrical approximation and its inverse matrix, and $\mathbf{K}_\alpha^{ab}$ denotes the components of some pseudo-stiffness matrix obtained by summing quantities evaluated at the Ith integration points of parent coordinates $\boldsymbol{\xi}_I$. The latter is computed and stored once and for all for each element for a given computational grid.

3.2.2. Surface fluxes

The discrete surface fluxes can be computed at each cell interface with the following quadrature

$$(\mathbf{F}_s)_{ia} = \sum_J \left(\bar{w}_J \Phi_a \boldsymbol{\mathcal{F}}_{i\alpha}\left(\mathbf{q}_h^-, \mathbf{q}_h^+\right) \mathcal{J} \frac{\partial \xi_m}{\partial X_\alpha} \mathcal{N}_m \right)(\boldsymbol{\xi}_J) \tag{33}$$

where Nanson's formula has been used for the transfer of the integrand to the spatial parent domain, with $\mathcal{N}$ being the local normal to the parent domain, and a dedicated integration rule is used for the interface. The interface fluxes $\boldsymbol{\mathcal{F}}_{i\alpha}\left(\mathbf{q}_h^-, \mathbf{q}_h^+\right)$ are computed from the solution of the following Riemann problem, defined with the quasi-linear form (11) at each integration point of parent coordinate $\boldsymbol{\xi}_J$ of a cell interface

$$\begin{aligned} &\frac{\partial \mathbf{q}}{\partial \tau} + \frac{\partial \boldsymbol{\mathcal{F}}_N}{\partial X_N} = 0, \qquad X_N = \mathbf{X} \cdot \mathbf{N} \in]-\infty, +\infty[, \tau > 0 \\ &\begin{cases} \mathbf{q}(X_N, \tau = \tau_s) = \mathbf{q}_h^- & \text{if } X_N < 0 \\ \mathbf{q}(X_N, \tau = \tau_s) = \mathbf{q}_h^+ & \text{if } X_N > 0 \end{cases} \end{aligned} \tag{34}$$

where τ denotes some parent time coordinate, and $(\mathbf{q}_h^-, \mathbf{q}_h^+)$ are known data at the left and right sides of a given interface at intermediate time τ_s. A linearized Riemann solver [66] can be constructed by approximating the jacobian matrix $\boldsymbol{\mathcal{A}}_N = \boldsymbol{\mathcal{A}}_\alpha N_\alpha$ by a constant matrix $\underline{\boldsymbol{\mathcal{A}}}_N(\mathbf{q}_h^-, \mathbf{q}_h^+)$ in the vicinity of states $\mathbf{q}_h^-$ and $\mathbf{q}_h^+$. If that matrix correctly ensures hyperbolicity, namely it has real eigenvalues and a complete set of independent eigenvectors, and satisfies the consistency condition[40]

$$\underline{\boldsymbol{\mathcal{A}}}_N(\mathbf{q}, \mathbf{q}) = \boldsymbol{\mathcal{A}}_N(\mathbf{q}), \tag{35}$$

then the solution of problem (34) consists of M discontinuous waves emanating from the origin of the (X_N, τ) plane, with celerities c_i and associated right eigenvectors $\mathbf{r}_\mathbf{q}^{(i)}$, $1 \le i \le M$. The stationary solution is obtained for the ray $X_N/\tau = 0$ as

$$\mathbf{q}^* = \mathbf{q}_h^- + \sum_{\substack{i=1 \\ c_i<0}}^{M} \delta_i \mathbf{r}_\mathbf{q}^{(i)} = \mathbf{q}_h^+ - \sum_{\substack{i=1 \\ c_i>0}}^{M} \delta_i \mathbf{r}_\mathbf{q}^{(i)}, \tag{36}$$

where the wave strength coefficients δ_i can be computed from the solution of the following linear system

$$\mathbf{q}_h^+ - \mathbf{q}_h^- = \sum_{i=1}^{M} \delta_i \mathbf{r}_{\mathbf{q}}^{(i)}. \tag{37}$$

The interface fluxes $\mathcal{F}_{i\alpha}\left(\mathbf{q}^-, \mathbf{q}_h^+\right)$ appearing in the quadrature formula of surface fluxes (33) are then computed with the stationary solution $\mathbf{q}^*$

$$\mathcal{F}_{i\alpha}\left(\mathbf{q}_h^-, \mathbf{q}_h^+\right) = \mathcal{F}_{i\alpha}\left(\mathbf{q}^*\right), \tag{38}$$

also known as the Godunov flux[26].

3.3. Basic slope limiters

Although non-oscillatory solutions are mainly enforced in ADER-DGFEM through an *a posteriori* sub-cell WENO-FV-based limiter[21, 15], basic slope limiters with piecewise monotonic linear reconstruction[17, 38, 46] are used in this work for the sake of simplicity, although the former could also be adapted for ADER-DGMPM. The main idea is to enforce at some limiting points $\mathbf{X}_K$, $K \in \mathcal{V}$, such as the Gauss-Legendre integration points of an interface, the local maximum principle

$$\bar{\boldsymbol{\mathcal{U}}}_e^{\min} \leq \boldsymbol{\mathcal{U}}_e^n(\mathbf{X}_K) \leq \bar{\boldsymbol{\mathcal{U}}}_e^{\max}; \qquad \bar{\boldsymbol{\mathcal{U}}}_e^{\min} = \min_{j \in N_e} \bar{\boldsymbol{\mathcal{U}}}_j^n \; ; \; \bar{\boldsymbol{\mathcal{U}}}_e^{\max} = \max_{j \in N_e} \bar{\boldsymbol{\mathcal{U}}}_j^n \tag{39}$$

where $\bar{\boldsymbol{\mathcal{U}}}_e^n$ denotes the element average of the vector of conserved quantities $\boldsymbol{\mathcal{U}}$ in the element Ω_e at time t_n, and N_e are the set of indices of nearby elements of Ω_e, plus Ω_e itself. The piecewise monotonic linear reconstruction requires to compute a gradient, usually obtained by using a least square procedure using information from the current cell as well as values from nearby cells, whose solution reads

$$\nabla \bar{\boldsymbol{\mathcal{U}}}_e^n = \left[\sum_{\gamma=1}^{m} \boldsymbol{\nu}_{e\gamma} \otimes \boldsymbol{\nu}_{e\gamma}\right]^{-1} \sum_{\gamma=1}^{m} \left(\frac{\bar{\boldsymbol{\mathcal{U}}}_\gamma - \bar{\boldsymbol{\mathcal{U}}}_e}{d_{e\gamma}}\right) \otimes \boldsymbol{\nu}_{e\gamma} \quad ; \quad \boldsymbol{\nu}_{e\gamma} = \frac{\mathbf{X}_\gamma - \mathbf{X}_e}{d_{e\gamma}} \tag{40}$$

where $\mathbf{X}_\gamma$ and $\mathbf{X}_e$ are the coordinates of the centroids of grid cells γ and e, and $d_{e\gamma}$ their relative distance. The limited solution is reconstructued componentwise. It involves the reconstructed gradient (40), and a set of limiting coefficients associated with each component of System (5) gathered in the vector $\boldsymbol{\alpha}_e$, such that $\dim(\boldsymbol{\alpha}_e) = M$, where $\dim(\bullet)$ refers to the dimension of the quantity $(\bullet)$. The reconstructed limited solution reads:

$$\boldsymbol{\mathcal{U}}_{e,\lim}^n(\mathbf{X}) = \bar{\boldsymbol{\mathcal{U}}}_e^n + \mathrm{diag}(\boldsymbol{\alpha}_e) \cdot \nabla \bar{\boldsymbol{\mathcal{U}}}_e^n \cdot (\mathbf{X} - \mathbf{X}_e). \tag{41}$$

The limiting coefficients are defined as the componentwise minimum values among those computed for several limiting points of coordinates $\mathbf{X}_K$:

$$\boldsymbol{\alpha}_e = \min_{K \in \mathcal{V}} \boldsymbol{\alpha}_K, \tag{42}$$

where

$$\boldsymbol{\alpha}_K = \begin{cases} g\left(\frac{\bar{\boldsymbol{\mathcal{U}}}_e^{\max} - \bar{\boldsymbol{\mathcal{U}}}_e^n}{\boldsymbol{\mathcal{U}}_e^n(\mathbf{X}_K) - \bar{\boldsymbol{\mathcal{U}}}_e^n}\right) & \text{if } \boldsymbol{\mathcal{U}}_e^n(\mathbf{X}_K) - \bar{\boldsymbol{\mathcal{U}}}_e^n > 0 \\ g\left(\frac{\bar{\boldsymbol{\mathcal{U}}}_e^{\min} - \bar{\boldsymbol{\mathcal{U}}}_e^n}{\boldsymbol{\mathcal{U}}_e^n(\mathbf{X}_K) - \bar{\boldsymbol{\mathcal{U}}}_e^n}\right) & \text{if } \boldsymbol{\mathcal{U}}_e^n(\mathbf{X}_K) - \bar{\boldsymbol{\mathcal{U}}}_e^n < 0 \\ 1 & \text{if } \boldsymbol{\mathcal{U}}_e^n(\mathbf{X}_K) - \bar{\boldsymbol{\mathcal{U}}}_e^n = 0 \end{cases} \cdot \tag{43}$$

The function $g(x)$ denotes here a real-valued function associated with the limiter, hence Equation (43) is computed componentwise. The Barth-Jespersen[4] limiter is obtained for $g(x) = \min(1, x)$; that of Venkatakrishnan[70] for $g(x) = \dfrac{x^2 + 2x}{x^2 + x + 2}$.

4. Space-time ADER-DGMPM predictor

4.1. Space-time approximation of a local auxiliary problem

Following [22], one introduces the following local auxiliary Cauchy problem

$$\begin{aligned} &\frac{\partial \mathbf{u}}{\partial t} + \mathrm{DIV}\,\boldsymbol{\mathcal{F}} = 0, \quad \forall (\mathbf{X}, t) \in (\mathbb{R}^d \times [0, \Delta t]) \\ &\mathbf{u}(\mathbf{X}, 0) = \mathbf{U}_h(\mathbf{X}, t = t_n)|_{\Omega_e} \quad \forall \mathbf{X} \in \mathbb{R}^d \end{aligned} \tag{44}$$

which is assumed to be solved in an infinite medium, i.e. with no data coming neither from any boundaries nor from the neighboring grid cells. Practically speaking, the initial value problem (44) is solved within the space-time slab $\Omega_e \times [t_n, t_{n+1}]$, therefore its initial conditions are provided by the spatial approximation $\mathbf{U}_h(\mathbf{X}, t_n)|_{\Omega_e}$ reconstructed from the vector of conserved quantities $\mathbf{U}_p(t_n)$ known at time t_n *at each material point* $p = 1, \ldots, N_p$ of initial coordinates $\mathbf{X}_p$.

The following common space-time approximate solution $\mathbf{u}_h(\mathbf{X}, t)$ is provided by ADER-DGFEM[22, 15] to that of the local auxiliary problem (44)

$$\mathbf{u}_h(\mathbf{X}, t) = \sum_{l=1}^{N_{\mathrm{dofs}}} \theta_l(\mathbf{X}, t)\hat{\mathbf{u}}_l, \tag{45}$$

where $N_{\mathrm{dofs}} = (M+1)^{d+1}$ is the number of degrees of freedom of the approximation, d is the space dimension, and the multi-index $l = (l_0, l_1, l_2)$ (if $d = 2$) denotes the degrees of freedom associated with various space locations and intermediate times. More specifically, the space-time shape functions $\theta_l(\mathbf{X}, t)$ are usually constructed in the context of ADER-DGFEM by a classical tensorisation of one-dimensional Lagrange polynomials of degree N passing through $N+1$ Gauss-Legendre interpolation points, yielding $\theta_l(\mathbf{X}, t) = \varphi_{l_0}(\tau)\varphi_{l_1}(\xi)\varphi_{l_2}(\eta)$, and the time coordinate t is mapped to the reference time $\tau \in [0, 1]$, via $t = t_n + \tau \Delta t$.

However, since the computational domain is discretized within the context of DGMPM into a collection of material points (see Figure 1), the tensorisation of one-dimensional Lagrange polynomials associated with spatial coordinates cannot be pursued, since the location of those material points can be arbitrary within a grid cell. However, the tensorisation between spatial functions and the temporal one can be kept, giving the following space-time shape functions

$$\theta_l(\mathbf{X}, t) = \varphi_{l_0}(\tau)\chi_p(\xi, \eta), \tag{46}$$

where $\chi_p(\xi, \eta)$ denotes some multi-variate spatial shape function associated with *one material point* p lying in the grid cell Ω_e. As a consequence, the degrees of freedom $\hat{\mathbf{u}}_l$ appearing in the space-time approximation (45) are now defined *at material points*, at some intermediate time in the interval $[t_n, t_{n+1}]$. The approximation (45) is therefore quite different in the context of ADER-DGMPM with respect to that of ADER-DGFEM.

4.2. Forward mapping particle to grid via a Moving Least Square approximation

The Moving Least Square[60, 37] (MLS) approximation represents one method among many others to reconstruct functions from scattered data. It has been used to build approximations for many meshless methods[50, 6, 42, 52] from fields defined pointwise. It is therefore well suited to build the forward mapping particle to grid, through the construction of spatial shape functions $\chi_p(\xi, \eta)$. Notice that the use of MLS approximation has already been used in the context of the improved MPM in [27]. Here, it is rather derived in the context of ADER-DGMPM. The MLS approximation u_h of an any scalar field u is given by

$$u_h(\mathbf{X}) = \sum_{j=0}^{m} p_j(\mathbf{X})a_j(\mathbf{X}) = \mathbf{p}^T(\mathbf{X})\mathbf{a}(\mathbf{X}) \tag{47}$$

where $\mathbf{p}^T(\mathbf{X}) = [1 \quad X_1 \quad X_2 \quad X_1X_2 \quad X_1^2 \quad X_2^2 \quad \ldots]$ is a m-order polynomial (here Lagrange) basis in the two-dimensional setting and $\mathbf{a}(\mathbf{X}) = [a_0(\mathbf{X}) \quad a_1(\mathbf{X}) \quad \ldots a_m(\mathbf{X})]$ is a vector of coefficients obtained by minimizing the quadratic functional

$$J = \frac{1}{2}\sum_{p=1}^{N_p} w(\mathbf{X} - \mathbf{X}_p)\left[\mathbf{p}^T(\mathbf{X}_p)\mathbf{a}(\mathbf{X}_p) - \bar{u}_p\right]^2, \tag{48}$$

where $\bar{u}_p$ is the given data at point p, and $w(\mathbf{X}-\mathbf{X}_p)$ denotes a weight function with compact support. Once the functional (48) has been minimized, the solution coefficients $\mathbf{a} = \mathbf{A}^{-1}\mathbf{B}\bar{\mathbf{u}}$ can be introduced in the approximation (47) in order to obtain the MLS shape function associated with the material point p involved in space-time shape functions (46) of the predictor

$$\chi_p(\mathbf{X}) = \mathbf{p}^T(\mathbf{X}_p)[\mathbf{A}(\mathbf{X}_p)]^{-1}\mathbf{B}_p(\mathbf{X}_p), \tag{49}$$

where the matrices $\mathbf{A}$ and $\mathbf{B}$ are defined as

$$\mathbf{A}(\mathbf{X}) = \sum_{p=1}^{N_p} w(\mathbf{X}-\mathbf{X}_p)\mathbf{p}(\mathbf{X}_p)\mathbf{p}^T(\mathbf{X}_p)\,; \quad \mathbf{B}(\mathbf{X}) = \Big[w(\mathbf{X}-\mathbf{X}_1)\mathbf{p}(\mathbf{X}_1), \quad \dots \quad , w(\mathbf{X}-\mathbf{X}_{N_p})\mathbf{p}(\mathbf{X}_{N_p})\Big]. \tag{50}$$

The reconstructed MLS approximation of the vector of conserved quantities at time t_n from the pointwise values known at material points thus reads

$$\mathbf{U}_h(\mathbf{X}, t_n) = \sum_{p=1}^{N_p} \chi_p(\mathbf{X})\mathbf{U}_p^n, \tag{51}$$

which provides the initial conditions to the local Cauchy problem (44).

It is clear that the moment matrix $\mathbf{A}(\mathbf{X})$ (50) of size $m \times m$ should be invertible wherever the MLS shape functions are to be evaluated. On the one hand, a necessary condition for the moment matrix to be invertible is that $N_p \geq m$. On the other hand, pathological arrangements of material points leading to a singular matrix should be avoided, especially if $N_p = m$ (see [52] for more details on it), hence the locations of material points within the grid cell Ω_e may not be completely arbitrary.

The MLS shape function (49) relies on a weight function $w(\mathbf{X}-\mathbf{X}_p)$ which should satisfy a set of mathematical properties. Especially, it should be non-zero and positive only over a compact support, continuous, satisfy to some unity and Dirac delta conditions (see [6] for more details), and be a monotonically decreasing function of $r = \frac{\|\mathbf{X}-\mathbf{X}_p\|}{d_p}$, where d_p is the support size of the material point p. To fix ideas, one very common weight function is the cubic spline

$$w(r) = \begin{cases} \frac{2}{3} - 4r^2 + 4r^3, & r \leq \frac{1}{2} \\ \frac{4}{3} - 4r + 4r^2 - \frac{4}{3}r^3, & \frac{1}{2} < r \leq 1 \\ 0, & r > 1 \end{cases}, \tag{52}$$

but others with higher order of smoothness can be considered, see [6]. For multi-space dimensions, the weight function can be generated from a tensor product. For instance, in the two-dimensional setting it reads:

$$w(\mathbf{X}-\mathbf{X}_p) = w\left(\frac{|X_{1,p}-X_1|}{d_p^{X_1}}\right) w\left(\frac{|X_{2,p}-X_2|}{d_p^{X_2}}\right) \tag{53}$$

Basically, the support sizes $(d_p^{X_1}, d_p^{X_2})$, or smoothing lengths, are defined as the two dimensions of a quadrilateral element.

Note also that both MPM and DGMPM use Shepard's functions[60] for the particle to grid mapping, also known as MLS at order zero

$$\chi_p^0(\mathbf{X}) = \frac{w(\mathbf{X}-\mathbf{X}_p)}{\sum_q w(\mathbf{X}-\mathbf{X}_q)}, \tag{54}$$

coupled with a piecewise linear weight function (actually a "hat" function) over the compact support (see [27]). Higher order MLS approximation thus allows to get a higher order approximation for the DGMPM.

Finally, thanks to the total Lagrangian framework retained in Section 2, the material points of coordinates $\mathbf{X}_p$ are defined in the initial configuration Ω_0 of the body Ω. Hence, the MLS approximation (47) is computed once and for all for a given mesh, until the grid is discarded.

4.3. Local space-time DGMPM-predictor

Multiplying Equation (44) by the space-time shape function θ_k, and integrating over the space-time domain $\Omega_e \times [t_n, t_{n+1}]$ yields its integral form

$$\int_{t_n}^{t_{n+1}} \int_{\Omega_e} \theta_k \left(\frac{\partial \mathbf{u}_h}{\partial t} + \mathrm{DIV}\, \boldsymbol{\mathcal{F}} \right) dV dt = 0. \tag{55}$$

However, since an element local predictor solution is sought, no interactions with any neighbor element is required at this stage, which will be accounted for during the corrector stage (31) via the computation of interface fluxes. Hence no integration by parts in space is required, but rather an integration by parts in time of the first term gets rid of the time derivative of the sought predictor field. Then, once the integrals have been transfered to the parent domains of both space and time coordinates, and accounting for the approximation (45) valid for both the vector of conserved quantities $\mathbf{u}_h$ and the auxiliary vector $\mathbf{q}_h$, one gets the following discrete system of non-linear equations

$$\begin{aligned} &\left\{ \iint_{\square} \theta_k(\boldsymbol{\xi}, \tau = 1)\theta_l(\boldsymbol{\xi}, \tau = 1) \mathcal{J} d\boldsymbol{\xi} - \int_0^1 \iint_{\square} \frac{\partial \theta_k(\xi, \tau)}{\partial \tau} \theta_l(\boldsymbol{\xi}, \tau) \mathcal{J} d\boldsymbol{\xi} d\tau \right\} \hat{\mathbf{u}}_l \\ &\qquad = \iint_{\square} \theta_k(\boldsymbol{\xi}, \tau = 0) \chi_p(\boldsymbol{\xi}) \mathcal{J} d\boldsymbol{\xi} \mathbf{U}_p^n - \Delta t \int_0^1 \iint_{\square} \theta_k(\xi, \tau) \frac{\partial \theta_l(\boldsymbol{\xi}, \tau)}{\partial \xi_m} \frac{\partial \xi_m}{\partial X_\alpha} \mathcal{J} d\boldsymbol{\xi} d\tau \boldsymbol{\mathcal{F}}_\alpha(\hat{\mathbf{q}}_l), \end{aligned} \tag{56}$$

where the parent domain $\square$ associated with space coordinates may be defined as $[0, 1]^2$ or $[-1, 1]^2$, the initial conditions are reconstructed from the MLS approximation (51), and $\boldsymbol{\mathcal{F}}_\alpha(\hat{\mathbf{q}}_l)$ denotes the fluxes $\boldsymbol{\mathcal{F}}_\alpha = \boldsymbol{\mathcal{F}} \cdot \mathbf{E}_\alpha$ computed with the auxiliary vector $\hat{\mathbf{q}}_l$ associated with the lth degree of freedom. System (56) applies for each ith component $(\hat{u}_{il}, U_{ip}^n, \hat{q}_{il})$ of vectors $(\hat{\mathbf{u}}_l, \mathbf{U}_p^n, \hat{\mathbf{q}}_l)$, and can be recast in a more compact form as

$$\mathbf{S}_\tau \hat{\mathbf{u}} = \mathbf{R}_0 \mathbf{U}^n - \Delta t \sum_\alpha \mathbf{S}_\alpha \boldsymbol{\mathcal{F}}_\alpha(\hat{\mathbf{q}}) \tag{57}$$

where

$$\hat{\mathbf{u}} = [\hat{\mathbf{u}}_1 \quad \hat{\mathbf{u}}_2 \quad \dots \quad \hat{\mathbf{u}}_M]^T \quad ; \quad \hat{\mathbf{q}} = [\hat{\mathbf{q}}_1 \quad \hat{\mathbf{q}}_2 \quad \dots \quad \hat{\mathbf{q}}_M]^T \tag{58}$$

$$\mathbf{S}_\tau = \mathrm{diag}\left[\mathbf{S}_\tau^i, 1 \le i \le M\right] ; \left(\mathbf{S}_\tau^i\right)_{kl} = \left(\iint_{\square} \theta_k(\boldsymbol{\xi}, \tau = 1)\theta_l(\boldsymbol{\xi}, \tau = 1) \mathcal{J} d\boldsymbol{\xi} - \int_0^1 \iint_{\square} \frac{\partial \theta_k(\boldsymbol{\xi}, \tau)}{\partial \tau} \theta_l(\boldsymbol{\xi}, \tau) \mathcal{J} d\boldsymbol{\xi} d\tau \right) \tag{59}$$

$$\mathbf{R}_0 = \mathrm{diag}\left[\mathbf{R}_0^i, 1 \le i \le M\right] ; \left(\mathbf{R}_0^i\right)_{kp} = \iint_{\square} \theta_k(\boldsymbol{\xi}, \tau = 0) \chi_p(\boldsymbol{\xi}) \mathcal{J} d\boldsymbol{\xi} \tag{60}$$

$$\mathbf{S}_\alpha = \mathrm{diag}\left[\mathbf{S}_\alpha^i, 1 \le i \le M\right] ; \left(\mathbf{S}_\alpha^i\right)_{kl} = \int_0^1 \iint_{\square} \theta_k(\boldsymbol{\xi}, \tau) \frac{\partial \theta_l(\boldsymbol{\xi}, \tau)}{\partial \xi_m} \frac{\partial \xi_m}{\partial X_\alpha} \mathcal{J} d\boldsymbol{\xi} d\tau \tag{61}$$

provided $\hat{\mathbf{u}}_i$, $1 \le i \le M$ here denotes all degrees of freedom related to the component i of System (5), so that $\dim(\hat{\mathbf{u}}_i) = N_{\mathrm{dofs}}$, where $\dim(\bullet)$ refers to the dimension of the quantity $(\bullet)$. Conversely, $\hat{\mathbf{u}}_l$, $1 \le l \le N_{\mathrm{dofs}}$ refers to all components related to the lth degree of freedom, such that $\dim(\hat{\mathbf{u}}_l) = M$. The same definitions apply for $\hat{\mathbf{q}}_i$ and $\hat{\mathbf{q}}_l$.

System (57) is non-linear and should be solved on $\hat{\mathbf{u}}$ with an iterative process. It is usually solved by means of some fixed point algorithm (or Picard iterations, see e.g. [22]), such that the following update is provided at each iteration r of the computation

$$\hat{\mathbf{u}}^{(r+1)} = \mathbf{S}_\tau^{-1} \mathbf{R}_0 \mathbf{U}^n - \Delta t \sum_\alpha \mathbf{S}_\tau^{-1} \mathbf{S}_\alpha \boldsymbol{\mathcal{F}}_\alpha(\hat{\mathbf{q}}^{(r)}), \tag{62}$$

where the auxiliary vector $\hat{\mathbf{q}}^{(r)}$ has been computed from $\hat{\mathbf{u}}^{(r)}$ known at iteration r. Especially, stresses are computed from the deformation gradient plus a possible set of internal variables through constitutive updates which are performed *at material points*, at various intermediate times $\tau \in [0, 1]$ according to the index l of the associated degree of freedom. Notice that the iterative solution of the non-linear system (62) has been shown to be convergent[15]. Besides, since the matrix $\mathbf{S}_\tau^{-1}\mathbf{S}_\alpha$ is nilpotent[36], yielding all its eigenvalues to be zero, the convergence to the exact solution is guaranteed in a finite number of steps for linear homogeneous PDE. Figure 2 shows a sketch of the discretization of a model space-time control volume $C^n = (\xi, \eta, \tau) \in [-1, 1]^2 \times [0, 1]$, plotted with only two space

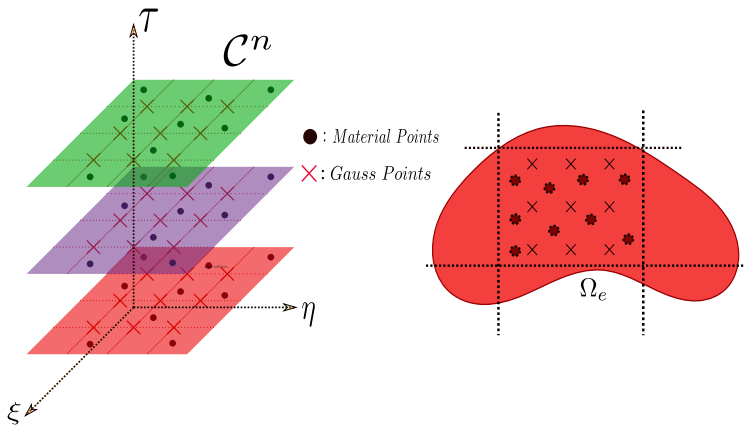

Figure 2: Discretization of a model space-time control volume $C^n = (\xi, \eta, \tau) \in [-1, 1]^2 \times [0, 1]$ with a quadratic approximation, plotted with only two space dimensions for visualization purpose.

dimensions for visualization purpose. Layers of 3×3 Gauss integration points and of the same set of material points are here defined in this example, at each intermediate time τ_s the chosen time integration rule consists of. The ADER approach permits to perform at the same time the particle to grid projection and the solution process of degrees of freedom associated with material points at those various intermediate times.

An efficient initial guess to the iterative solution process of the non-linear system (57) is of much importance to obtain a fast convergence. One possibility is to employ a second-order accurate MUSCL-Hancock-type approach[34] based on that of Van Leer[69], which basically consists in extrapolating the known approximation $\mathbf{U}_h(\mathbf{X}, t_n)$ (51) through some Taylor series expansion in time with a particular operator which here reduces to $-\mathrm{DIV}\,\mathcal{F}(\mathbf{Q}_h(\mathbf{X}, t_n))$:

$$\mathbf{u}_h(\mathbf{X}, t) = \mathbf{U}_h(\mathbf{X}, t_n) - (t - t_n)\mathrm{DIV}\,\mathcal{F}(\mathbf{Q}_h(\mathbf{X}, t_n)). \tag{63}$$

Therefore, provided the MLS approximation (51) is also applied to the auxiliary vector $\mathbf{Q}_h(\mathbf{X}, t_n)$, the initial guess (63) expresssed at each intermediate time τ_s reads

$$\hat{\mathbf{u}}_p(\tau_s) = \mathbf{U}_p^n - \Delta t \tau_s \sum_{q=1}^{N_p} \frac{\partial \chi_q}{\partial \xi_m}(\boldsymbol{\xi}_p)\frac{\partial \xi_m}{\partial X_\alpha}(\boldsymbol{\xi}_p)\mathcal{F}_\alpha(\mathbf{Q}_q^n) \tag{64}$$

where $\hat{\mathbf{u}}_p(\tau_s)$ denotes a vector consisting of all unknown components associated with the material point p, defined at the time slice τ_s. Notice that the initial guess (64) defined in the context of ADER-DGMPM requires to compute and to store (once and for all) the gradient of the MLS shape functions $\frac{\partial \chi_q}{\partial \xi_m}(\boldsymbol{\xi}_p)$ and the inverse jacobian matrix $\frac{\partial \xi_m}{\partial X_\alpha}(\boldsymbol{\xi}_p)$ expressed at material points $p = 1, \ldots, N_p$ of spatial parent coordinates $\boldsymbol{\xi}_p$.

Remark 1. While the updated solution in RK-DGFEM methods is computed in a recursive manner at each stage, the ADER approach provides a space-time approximation on the slab $\Omega_e \times [t_n, t_{n+1}]$ computed purely locally at once in an implicit manner. On the one hand, it avoids communications at each RK stage over the whole computational grid in a context of parallel implementation, and may allow for a simple time-accurate local time stepping. On the other hand, the sole predictor approximation requires a local implicit solution procedure, letting the global update on the grid (31) to be still time explicit.

In the context of DGMPM, RK methods may not appear as the best suited time integrators. Indeed, since the stresses should be updated on the grid at intermediate RK stages, either it would require to transfer internal variables from material points to the computational grid in order to perform constitutive update, or back and forth transfers of strains or stresses between material points and grid nodes should be carried out at each intermediate RK stage if internal variables are let at material points for constitutive updates. In both cases, additional numerical diffusion would be added in the scheme, which is not desirable. When coupled with DGMPM, ADER hence provides a suitable

framework to circumvent the above issues encountered with RK time integrators, especially when including Moving Least Square shape functions as the spatial contribution to the space-time approximation of the predictor field.

Remark 2. The computation of integrals (59), (60), (61) require to map back the coordinates of the material points from the initial configuration to the parent domain, and therefore to compute the associated geometrical inverse mapping. This is straightforward for rectangular grids, but may be costly for non-uniform quadrilateral grids since it requires the solution of a non-linear system of equations. Another possibility is to define the position of material points in the parent domain of each grid cell, and to only use the direct mapping to get their associated initial coordinates. In that last case, the computation of MLS shape functions (49) and of the weight function (53) can directly be computed with the parent coordinates $\boldsymbol{\xi}$, while the support sizes are defined as the lengths of the parent element.

4.4. Back-mapping grid to particles

Once the solution (31) has been updated on the grid, it is projected back to material points. Various back-mappings can be considered. The first one is a simple interpolation using the discontinuous Galerkin approximation (26)

$$\boldsymbol{\mathcal{U}}_h(\mathbf{X}_p, t_{n+1}) = \sum_{b=1}^{N_n} \Phi_b(\mathbf{X}_p) \hat{\boldsymbol{\mathcal{U}}}_b^{n+1} \tag{65}$$

for every material point $p = 1, \dots, N_p$ lying in each grid cell e. This is known as the PIC[28] (Particle-In-Cell) method. Another one is the FLIP[14] (Fluid Implicit Method), which rather amounts to interpolate the increment of the solution field over the time step back to material points:

$$\boldsymbol{\mathcal{U}}_h(\mathbf{X}_p, t_{n+1}) = \boldsymbol{\mathcal{U}}_h(\mathbf{X}_p, t_n) + \sum_{b=1}^{N_n} \Phi_b(\mathbf{X}_p)(\hat{\boldsymbol{\mathcal{U}}}_b^{n+1} - \hat{\boldsymbol{\mathcal{U}}}_b^{n}). \tag{66}$$

It is known to be less diffusive than PIC, at least in the MPM context. However, other types of back-mapping technique exist, such as XPIC[29], which may also be used in the context of ADER-DGMPM.

4.5. ADER-DGMPM solution scheme

Assume that for every material point $p = 1, \dots, N_p$ lying in each grid cell Ω_e, $e = 1, \dots, N_e$, the vector of conserved quantities $\mathbf{U}_p^n$ as well as the auxiliary vector $\mathbf{Q}_p^n$ are known at time t_n. After a stage of pre-processing of some quantities before the time loop, the computing procedure of ADER-DGMPM on the time increment $[t_n, t_{n+1}]$ mainly consists of three big steps. First, the ADER method permits to perform at the same time the forward projection of various fields from material points to the grid and the local solution process of the predictor field $\mathbf{u}_h(\mathbf{X}, t)$ (45) and its associated auxiliary vector $\mathbf{q}_h(\mathbf{X}, t)$ on each space-time slab $\Omega_e \times [t_n, t_{n+1}]$. Second, the vector of conserved quantities $\boldsymbol{\mathcal{U}}_h(\mathbf{X}, t_n)$ defined on the computational grid is updated cellwise via the corrector step. At last, a back projection from the grid to material points and a constitutive update permits to update the vectors $\mathbf{U}_p^{n+1}$ and $\mathbf{Q}_p^{n+1}$ at time t_{n+1} at each material point p.

Pre-processing step

Once the initial configuration Ω_0 of the body Ω has been discretized into a collection of material points, and a dedicated mapping between those points and each cell of a computational grid has been performed, some pre-processing operations can be carried out. Especially, since a total Lagrangian approach is followed here, many matrices can be computed and stored once and for all. On the one hand, the definition of the sole computational mesh and the associated integration rules permits to compute once and for all some elements of approximation at quadrature points (gradients of the nodal-DG shape functions, inverse mapping and associated determinant of the geometrical approximation) and then compute the pseudo-stiffness matrices $\mathbf{K}_\alpha^{ab}$ (32), as well as the mass matrix $\boldsymbol{\mathcal{M}}$ (29) which can be factorized. On the other hand, the mapping known between material points and the grid permits to compute cellwise the MLS shape functions (49) at space quadrature points, then to compute the space-time shape functions $\theta_l(\boldsymbol{\xi}, t)$ (46) and their space and time derivatives at space-time quadrature points or at particular end times of the time parent domain. From the latters, the matrices $\mathbf{S}_\tau^{-1}\mathbf{R}_0$ and $\mathbf{S}_\tau^{-1}\mathbf{S}_\alpha$ involved in the predictor step and appearing in the recurrence formula (62) are computed once and for all and stored.

Processing step

For each time step, the following processing steps are in order:

1. Compute the critical time step according to the CFL condition associated with DG schemes[17]:

$$\Delta t \leq \text{CFL} \frac{h_{\min}}{(2P+1)|\lambda_{\max}|} \tag{67}$$

where CFL is the Courant number, P is the polynomial order of the approximation, $h_{\min}$ is the minimum characteristic mesh-size, and $|\lambda_{\max}|$ is the maximum wavespeed. The characteristic speeds are computed from the eigenvalues of the acoustic tensor $\mathbf{C}_{NN}$ (24) depending on the deformation gradient $\mathbf{F}^n$ at time t_n. Notice that when applied to ADER-DGFEM, the values of the CFL number must be slightly reduced with respect to these associated with DGFEM for increasing orders of approximation, see [19, 22] for more details.

2. **Space-time predictor step**
   (a) Compute an initial guess $\hat{\mathbf{u}}_p(\tau_s)$ for each material point p at each intermediate time τ_s of the time integration rule with the explicit second order accurate Taylor expansion (64), from the data $(\mathbf{U}_p^n, \mathbf{Q}_p^n)$ known at material points at time t_n. The associated auxiliary vector $\hat{\mathbf{q}}_p(\tau_s)$ is computed via a constitutive update of stresses.
   (b) at each iteration r of the iterative process,
      i. Compute the fluxes $\boldsymbol{\mathcal{F}}_\alpha(\hat{\mathbf{q}}_l^{(r)})$ for each space-time degree of freedom l, $1 \leq l \leq N_{\text{dofs}}$.
      ii. Update $\hat{\mathbf{u}}^{(r+1)}$ with the recurrence formula (62).
      iii. Update the auxiliary vector $\hat{\mathbf{q}}^{(r+1)}$ from $\hat{\mathbf{u}}^{(r+1)}$. A constitutive update is performed for each degree of freedom l, that is for all *material points* $p = 1, \ldots, N_p$ and for all intermediate times s to update stresses $\mathbf{P}^{(r+1)}$ from the deformation gradient $\mathbf{F}^{(r+1)}$ contained in the vector $\hat{\mathbf{u}}^{(r+1)}$ and eventually internal variables known at material points at time t_n.
   (c) At convergence, the space-time approximations $\mathbf{u}_h(\mathbf{X}, t)$ (45) and $\mathbf{q}_h(\mathbf{X}, t)$ are known in $\Omega_e \times [t_n, t_{n+1}]$, and are especially expressed at space-time quadrature points for the next corrector step.

3. **Corrector step**
   (a) At each intermediate time τ_s,
      i. Compute the discrete volume fluxes $\mathbf{F}_v(\hat{\mathbf{q}}(\tau_s))$ with Equation (32).
      ii. Solve the approximate Riemann problem (34) with the jacobian matrix (35) at each cell interface of the mesh. Wave strength coefficients are solution of Equation (37), the stationary solution $\hat{\mathbf{q}}^*(\tau_s)$ follows from Equation (36), from which the interface fluxes $\boldsymbol{\mathcal{F}}_\alpha(\hat{\mathbf{q}}^*(\tau_s))$ are obtained with Equation (38).
      iii. Compute the discrete surface fluxes $\mathbf{F}_s(\hat{\mathbf{q}}^*(\tau_s))$ at each side of each interface of the mesh with the quadrature formula (33). Boundary conditions are enforced through the definition of ghost states at boundary interfaces.
   (b) Update the nodal degrees of freedom $\hat{\boldsymbol{\mathcal{U}}}_{n+1}$ at time t_{n+1} with the quadrature formula (31).
   (c) Apply slope limiters by reconstructing a limited piecewise monotonic linear solution $\boldsymbol{\mathcal{U}}_{e,\text{lim}}^n(\mathbf{X})$ with Equation (41).

4. **Back-mapping grid to particles**
   (a) Back-projection of the updated limited solution $\boldsymbol{\mathcal{U}}_{e,\text{lim}}^n(\mathbf{X})$ from interpolation points to material points using a classical interpolation (PIC) (65) or the FLIP back-mapping (66).
   (b) Constitutive updates are performed at material points from updated deformation gradients $\mathbf{F}_p^{n+1}$ contained in the vector $\mathbf{U}_p^{n+1}$, and eventually internal variables known at material points at time t_n. The stresses $\mathbf{P}_{n+1}$ are updated with Equation (20), eventually internal variables may also be updated at time t_{n+1}.

5. At this stage, and if required, the arbitrary computational grid inherited from MPM may be discarded, and rebuilt for any purpose. Especially, the construction of a new mesh may be motivated by the improvement of the approximation locally (for shock-capturing purpose), or for the sake of large deformations which have occurred and require a better mesh. Notice that reconstructing a new grid require to redo the whole pre-processing step before moving to the next time step.

4.6. Summary

It is worthwhile to summarize the novelties brought by ADER-DGMPM with respect to ADER-DGFEM:

1. The presence of material points in the ADER-DGMPM implies the definition of forward and back mappings between material points and the computational grid. The forward mapping is achieved via an MLS space approximation during the predictor stage, associated with degrees of freedom of the predictor now defined at material points and not at interpolation points as in ADER-DGFEM. The back mapping amounts to interpolate either the DGFEM solution (PIC) or its increment over the time step (FLIP) to transfer quantities from the interpolation points back to material points.
2. The constitutive updates are now only performed at material points, either during the predictor stage (at each iteration) or after the back-mapping. The computational grid becomes arbitrary, and can be discarded once the solution has been updated at material points. No step of projection of internal variables from one grid to another is required as in classical mesh-based methods.
3. ADER-DGMPM can reduce to the first-order DGMPM if wished, which thus represents a lower limit (actually of first-order accuracy) to the approximation of arbitrary high order of ADER-DGMPM. This can be achieved by changing the order of the MLS approximation (actually using Shepard's functions (54)) and using an integration rule based on material points[55, 56] rather than on Gauss-Legendre integration points. The main interest of the existence of such first-order accurate lower limit lies in that it can provide a monotone approximation, which appears as another way of achieving a non-oscillatory solution in the vicinity of shocks than using limiters. Moreover, if the grid is adapted so that a cell only consists of one material point, the usual upwind scheme is retrieved[57], with the associated optimal CFL condition[40].
4. For the sake of simplicity, a classical slope limiter has been kept in the present version of ADER-DGMPM, although an analog WENO-FV subcell limiter as used for ADER-DGFEM could also be developed for ADER-DGMPM.

5. Numerical examples

5.1. Convergence analysis on a two-dimensional square domain

We first consider smooth solutions for convergence analysis purpose of the ADER-DGMPM, obtained in the plane and small strains, isothermal, linear and isotropic elastodynamic framework. One considers a square computational domain of side length equal to $l = 1$m, with symmetry conditions set on its left and bottom sides, and traction-free prescribed on its top and right sides. This test case is similar to the one presented in [38], but with different boundary conditions. The following function

$$f(x_1, x_2) = \frac{U_0 \pi}{2} \cos\left(\frac{\pi x_1}{2}\right) \sin\left(\frac{\pi x_2}{2}\right), \tag{68}$$

with $U_0 = 5 \cdot 10^{-4}$ serves as an initial condition for the strain field, which reads at time $t = 0$ as

$$\boldsymbol{\varepsilon}(\mathbf{x}, t = 0) = f(x_1, x_2)\,(\mathbf{e}_1 \otimes \mathbf{e}_1 - \mathbf{e}_2 \otimes \mathbf{e}_2), \tag{69}$$

from which the initial stresses follow from the elastic law, while the velocity field vanishes initially. The analysis is here conducted with steel-like material parameters, more precisely with Young modulus $E = 2 \cdot 10^{11}$ Pa, Poisson's ratio $\nu = 0.3$ and mass density $\rho = 7800$ kg.m^{-3}. The convergence analysis is carried out with grids consisting of N_e elements per side ($N_e = 5, 10, 15, 25, 50$), with respect to a reference solution computed with a finer mesh of 100 cells per side. As a matter of illustration, Figure 3 shows the map of the first component of the velocity field of the reference solution at time $t = 6.8084 \cdot 10^{-6}$ seconds, computed with bi-quadratic polynomial order in space (S2) and quadratic one in time (T2).

The convergence curves of the relative errors in L^2 norm of the strain component ε_{11}, the Cauchy stress component σ_{11}, and of the velocity component V_1 as a function of the grid size Δx are here considered and shown in Figure 4, but are also representative of other fields. More precisely, bi-linear polynomial order in space (S1) and linear one in time (T1) are used for convergence curves shown in Figure 4a, bi-quadratic in space (S2) and quadratic in time

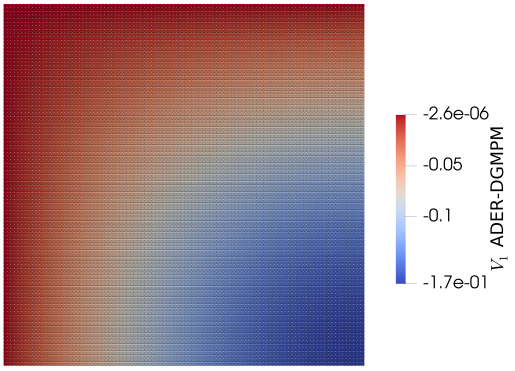

Figure 3: Reference solution of ADER-DGMPM computed with a bi-quadratic approximation in space (S2) and quadratic in time (T2): map of the first component of the velocity field at time $t = 6.8084 \cdot 10^{-6}$ seconds.

(T2) for these shown in Figure 4b, and bi-cubic in space (S3) and cubic in time (T3) for those shown in Figure 4c. For comparison purpose, convergence curves are plotted for RK-DGFEM, ADER-DGFEM and ADER-DGMPM methods.The PIC back-mapping (65) is used with ADER-DGMPM. Gauss-Legendre interpolation points mapped on the spatial parent domain $[0, 1]^2$ are considered for RK-DGFEM and ADER-DGFEM. A set of tensored material points are defined cellwise in the same parent domain for ADER-DGMPM, so that their parent coordinates are $\left\{\frac{1}{4}, \frac{3}{4}\right\}^2$, $\left\{\frac{1}{4}, \frac{1}{2}, \frac{3}{4}\right\}^2$, $\left\{\frac{1}{5}, \frac{2}{5}, \frac{3}{5}, \frac{4}{5}\right\}^2$ when combined with the bi-linear, bi-quadratic and bi-cubic polynomial orders respectively. The Moving Least Square approximation (see Section 4.2) is computed with a cubic spline (52) when the polynomial order is lower or equal than two, and with a quartic one (see [52, Eq. (3)]) for higher order, with a support size equal to the side length of the parent quadrilateral domain. Time integration is performed with a Courant number CFL set at 0.2, with a TVD-RK2 time scheme to compute the S1T1 solution of RK-DGFEM, and a RK4 to compute higher ones (S2T2 and S3T3). The relative errors shown in Figure 4 are computed at a fixed time. Typically, for a grid mesh of N_e elements per side, $N_t = N_e$ times steps are computed, leading to the same final instant for fixed CFL number and material parameters. However, since the critical time step (67) associated with the CFL condition depends on the order of approximation in DG methods, various orders give various final end times, which are approximately $\{2.76 \times 10^{-4}, 1.53 \times 10^{-4}, 4.89 \times 10^{-6}\}$ seconds for {S1T1,S2T2,S3T3} approximate solutions respectively.

The expected convergence rates of $(\Delta x)^{P+1}$, where P is the polynomial order, are correctly retrieved for all methods and for the various approximation orders. Namely, convergence rates of two, three and four are shown in Figures 4a, 4b and 4c, respectively associated with polynomial orders of one, two and three. All convergence curves are very close, and the constant do not differ much between the various numerical methods.

Next, this two-dimensional square problem is also used to quantify the diffusive aspects of the various methods. Notice that since the solution is smooth, no limiter is used. S1T1 approximations are used, with a discretization $N_e = 50, N_t = 3N_e$, and a CFL number set at 0.5. Figure 5 shows the time evolutions of the dimensionless total energy, namely the ratio of the total energy at current time t to its initial value $\frac{W_{\text{tot}}(t)}{W_{\text{tot}}(t=0)}$, when computed with the various methods. In addition, both PIC (65) and FLIP (66) back-mappings are considered when used together with ADER-DGMPM. It is clearly observed that (i) all methods are relatively few diffusive, the dimensionless total energy decreases at most of an amount of the order of 10^{-4} on the time interval of study for this smooth solution, (ii) all ADER schemes appear almost superposed and slightly more diffusive than TVD-RK2-DGFEM. A zoom allows to observe more precisely that PIC and FLIP appear almost superposed and that ADER-DGFEM lies a little bit above results of ADER-DGMPM. Hence, when the formulation relies on the first order system (5), and is solved with a DG approximation and an ADER time integrator, PIC and FLIP do not seem to have the same influence on diffusive aspects as in the original MPM. Besides, the MLS approximation in the ADER-DGMPM predictor does not seem to add much numerical diffusion with respect to ADER-DGFEM. In the sequel, ADER-DGMPM will be computed with PIC back-mapping.

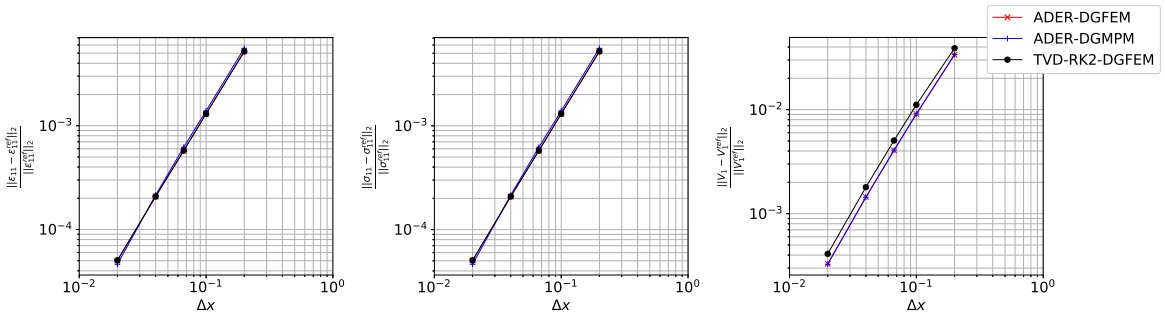

(a) Linear polynomial order (approximation S1T1).

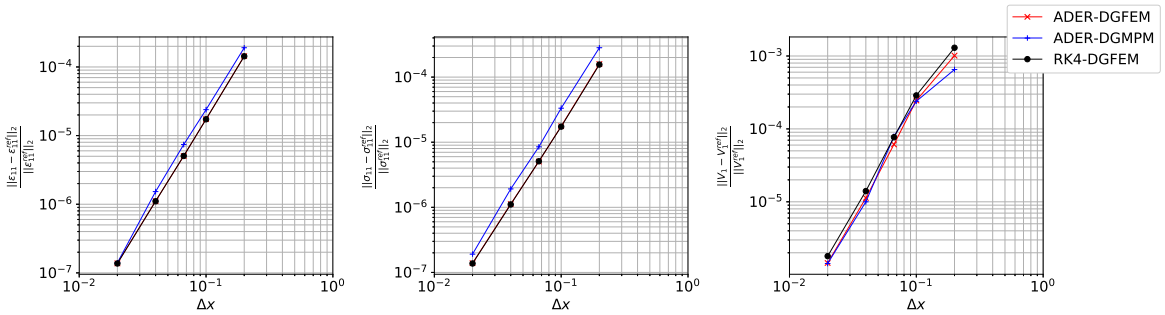

(b) Quadratic polynomial order (approximation S2T2).

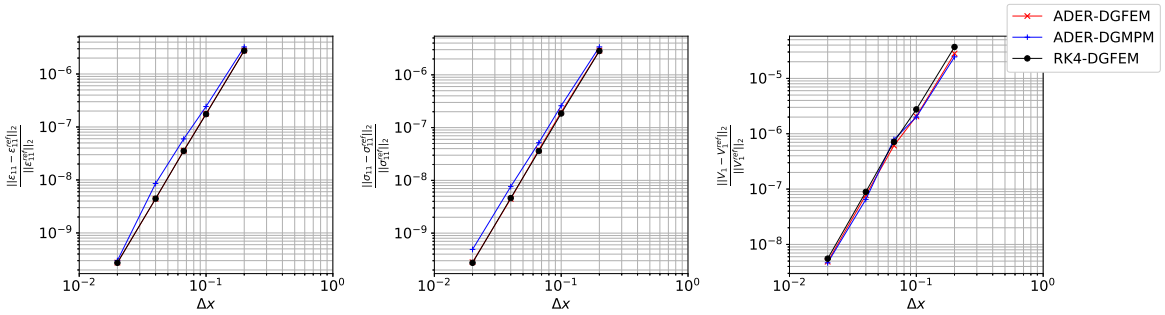

(c) Cubic polynomial order (approximation S3T3).

Figure 4: Convergence curves of the relative errors of fields $(\sigma_{11}, \varepsilon_{11}, V_1)$ in L^2 norm, computed for various approximation orders, and for RK-DGFEM, ADER-DGFEM and ADER-DGMPM.

5.2. LASAT-like test

Let us now consider the bidimensional square domain of side length l shown in Figure 6, submitted to an impact on a part of its left face, by means of a step function of a pressure $p(t)$ at time $t = 0$, which is released after a time $t_u = l/c_P$ where c_P is the pressure sound speed. A symmetry condition is considered on the bottom side, free boundaries are set at the right face and on the remaining part of the left one, and a perfect transmission condition is set on its top face. This problem is treated in the bidimensional plane and large strain framework. It can also be thought to approximate the conditions of a laser shock adhesion test (LASAT) [3]. In the latter, a laser pulse is applied on a small area of one side of a flat sheet in order to test the adhesion of some intermediate layer of the sheet thanks to a tensile normal stress which is generated at the crossing of two unloading waves, one arising from the unloading of the applied pressure, the other from the free boundary set at the opposite side. A basic constitutive response is here considered, consisting of a quadratic volumetric part of the energy (16) plus a neo-Hookean shear energy (19), associated with the same material parameters than those used in Section 5.1.

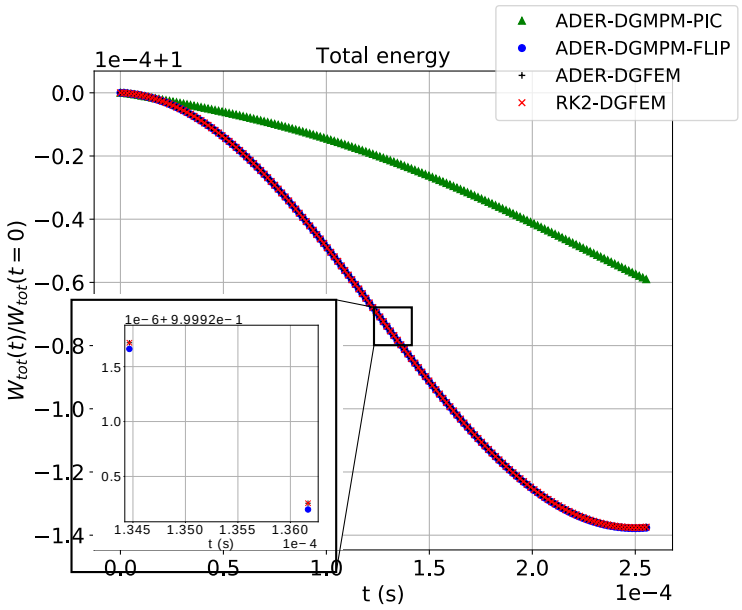

Figure 5: Time evolutions of the dimensionless total energy computed with the various methods.

Figure 7 shows the maps of the Cauchy stress component σ_{11} plotted in the current configuration of the square computational domain at two different times, computed with TVD-RK2-DGFEM, ADER-DGFEM and ADER-DGMPM. Results are computed with a CFL number set at 0.35, and with a bi-linear approximation in space (S1), and a linear one in time (T1) for ADER schemes. For comparison purpose, maps of fields are plotted by making a pointwise extraction either at Gauss-Legendre interpolation points for TVD-RK2-DGFEM and ADER-DGFEM, or at material points for ADER-DGMPM. Especially, Figure 7a shows the rightward propagation of the first compression shock wave through the thickness of the specimen. The capturing of its front is performed in a very similar manner by all numerical schemes in few elements. This can be viewed in Figure 8a, in which the plot of the Cauchy stress component σ_{11} is evaluated over the bottom line at the same instant for all methods. Since maps are defined with

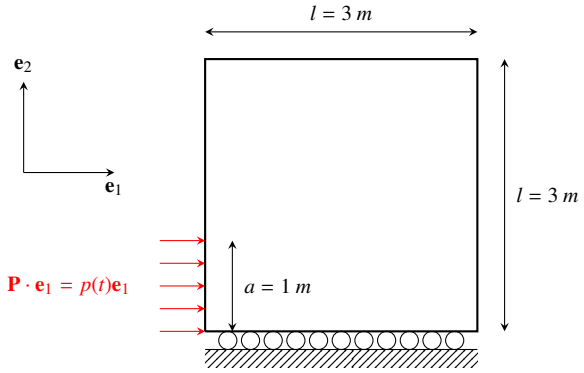

Figure 6: Partial impact on a two-dimensional square computational domain.

pointwise data in Figure 7, plots in Figure 8 are achieved thanks to a point-line interpolator available in the software Paraview[1]. Figure 7b shows a tensile normal stress that has occurred within the specimen after the crossing of two unloading waves. More precisely, at time $t \approx 1.14 \cdot 10^{-3}$ seconds, the tensile stress area is currently being reduced by two rightward and leftward unloading waves travelling towards each other. Once crossed, these two waves will then generate a compression area. The contour of the initial configuration of the square domain is also shown in Figure

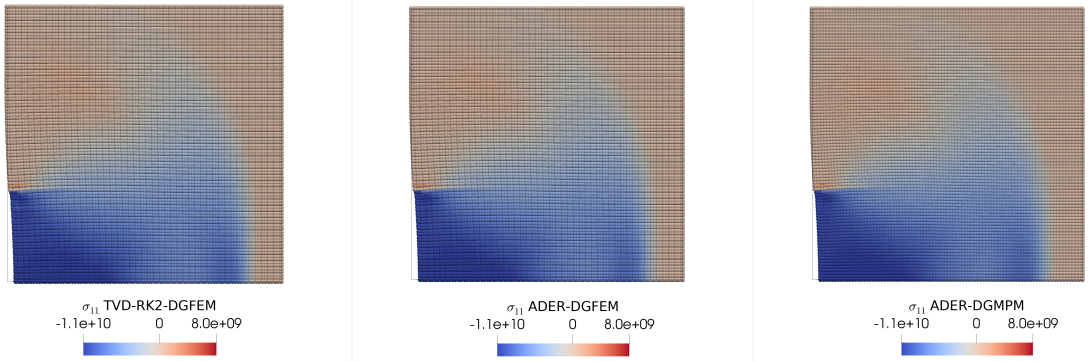

(a) $t \approx 4.25 \cdot 10^{-4}$ seconds.

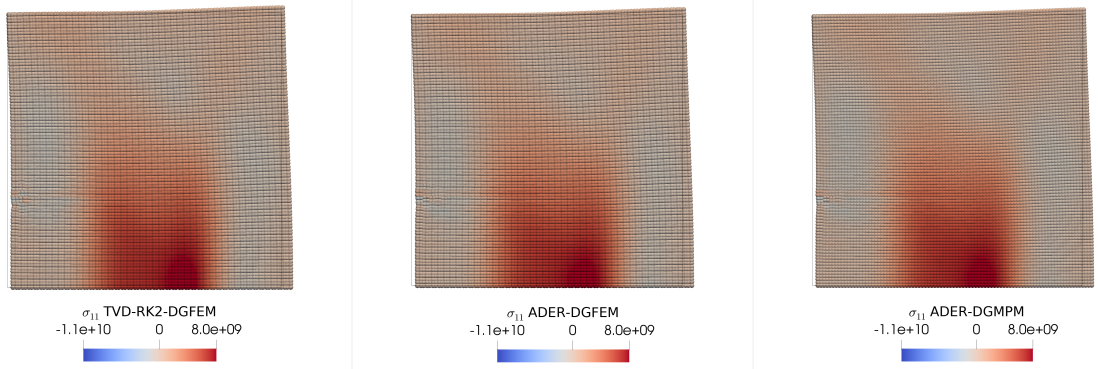

(b) $t \approx 1.14 \cdot 10^{-3}$ seconds.

Figure 7: Maps of the Cauchy stress component σ_{11} plotted in the current configuration of the square computational domain at various times, computed with TVD-RK2-DGFEM, ADER-DGFEM and ADER-DGMPM. Results are obtained with a bi-linear polynomial order in space (S1), and linear one in time (T1) for ADER schemes. Maps are made with pointwise extraction of fields either at Gauss-Legendre interpolation points (for TVD-RK2-DGFEM and ADER-DGFEM), or at material points (ADER-DGMPM).

7, so that its displacement is easily seen. Finally, Figure 8b shows the tensile normal stress state occurring at time $t \approx 1.14 \cdot 10^{-3}$ seconds. A very good correlation is also observed between the various numerical solutions.

5.3. Multi-holed elementary cell

A last example involving large strains pertains to a multi-holed elementary rectangular domain submitted to some impact loading, which is extracted from [33]. Figure 9 shows the computational domain and associated boundary conditions. It is drilled with several circular holes where free boundary conditions are considered. Symmetry conditions are set at the top, left and bottom sides of the domain, and a step function of a leftward velocity $-\bar{v}\mathbf{e}_1$ is applied on the right side of the domain at time $t = 0$. The numerical values of the geometrical and loading parameters are gathered in Table 1. Such geometry also permits to show the behaviour of the proposed method when used with non-uniform quadrilateral grids. This problem is also treated in the bidimensional plane and large strain framework, starting from a natural initial state, and considering the same hyperelastic constitutive response than the one used in Section 5.2.

Figure 10 shows the maps of the Cauchy stress component σ_{11} plotted at two different times in the current configuration of the multi-holed computational domain, computed with TVD-RK2-DGFEM, ADER-DGFEM and ADER-DGMPM, coupled to a bi-linear approximation in space (S1) and a linear one in time (T1) for ADER schemes. Time advancement is performed with a CFL number set at 0.2. A very good agreement is observed between the various numerical solutions at the two different times. This is also emphasized in Figure 11 which shows the plots of the velocity

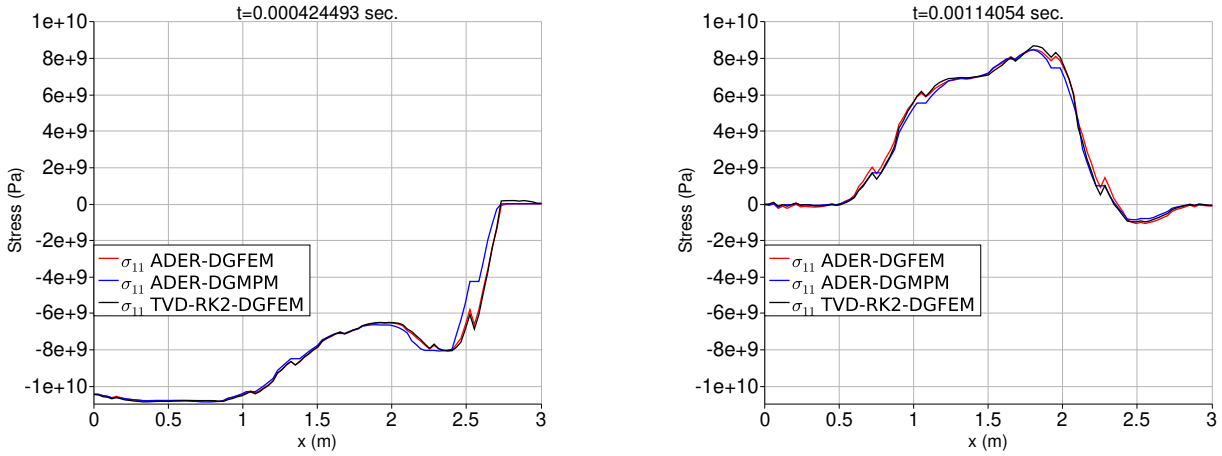

(a) $t \approx 4.25 \cdot 10^{-4}$ seconds.

(b) $t \approx 1.14 \cdot 10^{-3}$ seconds.

Figure 8: Plots of the Cauchy stress component σ_{11} along the bottom line of the square computational domain at various times, computed with TVD-RK2-DGFEM, ADER-DGFEM and ADER-DGMPM. Results are obtained with a bi-linear polynomial order in space (S1), and linear one in time (T1) for ADER schemes.

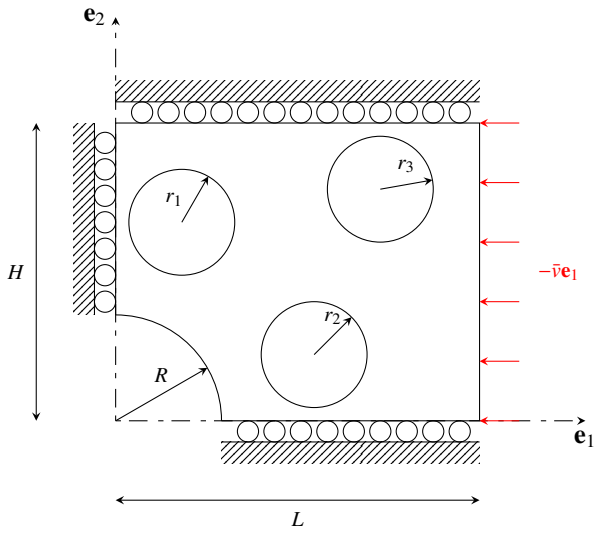

Figure 9: Sketch of the computational domain of the multi-holed elementary cell. Holes $1, 2, 3$ of radii $r = r_1 = r_2 = r_3$ are centered at locations $(w, 3w)$, $(3w, w)$ and $\left(4w, \frac{7w}{2}\right)$ respectively, where $w \in \left]\frac{R}{3}, \min\left(\frac{2}{7}(H-r), \frac{(L-r)}{4}\right)\right[$ is a parameter.

Geometry	$R = 8 \times 10^{-3}$ m $\quad r = 4 \times 10^{-3}$ m $\quad w = 5 \times 10^{-3}$ m $\quad L = \dfrac{11w}{2} \quad H = \dfrac{9w}{2}$
Loading	$\bar{v} = 300$ m.s^{-1}

Table 1: Geometrical and loading parameters for the multi-holed medium test case.

component V_1 evaluated along the bottom line of the computational domain for the various numerical solutions. This problem is challenging since holes tend to depart from a circular profile as strains increase, as shown in Figure 10b.

Figure 12 shows the same numerical simulation, but now computed with a bi-quadratic approximation in space

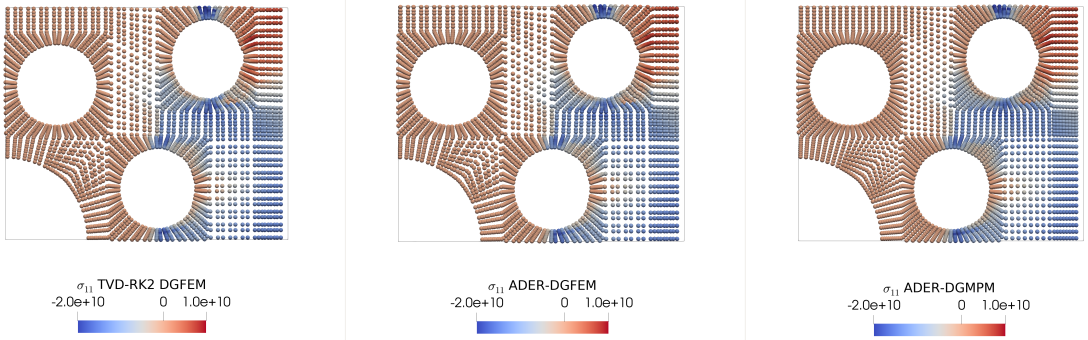

(a) $t \approx 2.39 \cdot 10^{-6}$ seconds.

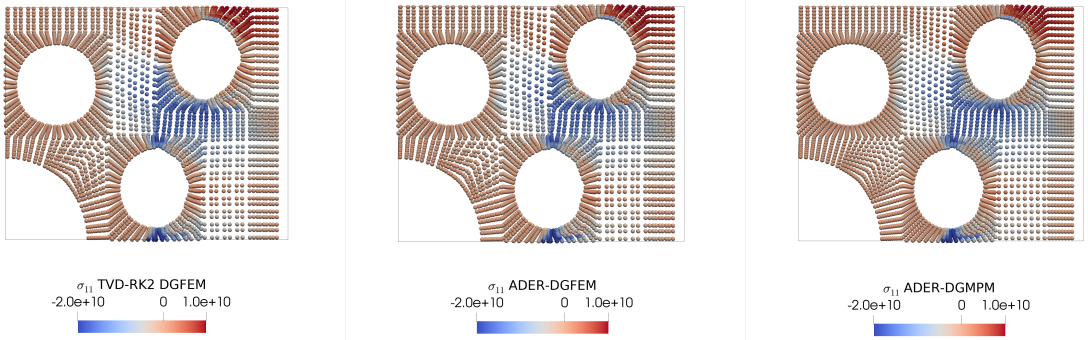

(b) $t \approx 3.63 \cdot 10^{-6}$ seconds.

Figure 10: Maps of the Cauchy stress component σ_{11} plotted in the current configuration of the multi-holed elementary cell at various times, computed with TVD-RK2-DGFEM, ADER-DGFEM and ADER-DGMPM. Results are obtained with a bi-linear polynomial order in space (S1), and linear one in time (T1) for ADER schemes. Maps are made with pointwise extraction of fields either at Gauss-Legendre interpolation points (for TVD-RK2-DGFEM and ADER-DGFEM), or at material points (ADER-DGMPM).

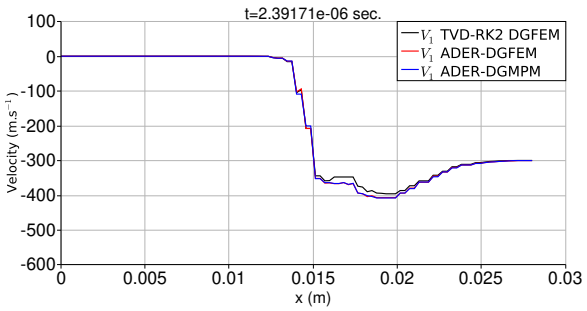

(a) $t \approx 2.39 \cdot 10^{-6}$ seconds.

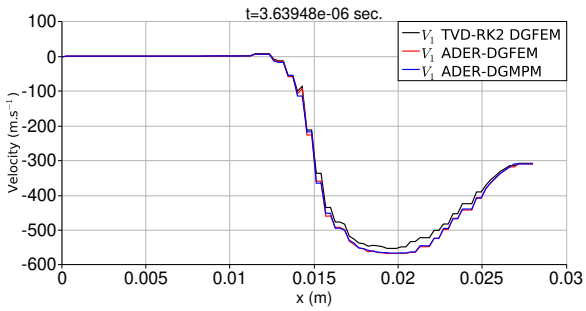

(b) $t \approx 3.63 \cdot 10^{-6}$ seconds.

Figure 11: Plots of the velocity component V_1 along the bottom line of the multi-holed medium at various times, computed with TVD-RK2-DGFEM, ADER-DGFEM and ADER-DGMPM. Results are obtained with a bi-linear polynomial order in space (S1), and linear one in time (T1) for ADER schemes.

(S2) for all methods, hence resulting in much more computation points, a quadratic one in time (T2) for ADER schemes, and a RK4 time integrator for RK-DGFEM. The same comments than the aforementioned ones still hold. The maps of stresses seen in Figure 12a show a very good correlation between the various numerical solutions, as well as velocity profiles shown in Figure 13. Besides the different time integration schemes and spatial discretizations

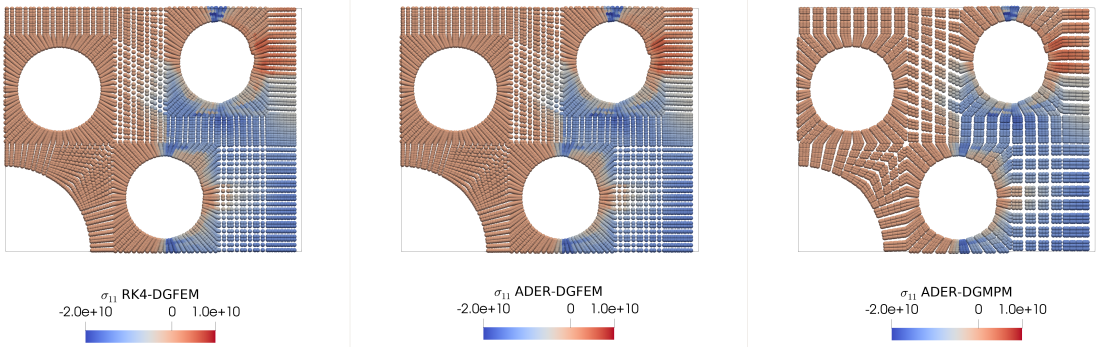

(a) $t \approx 2.39 \cdot 10^{-6}$ seconds.

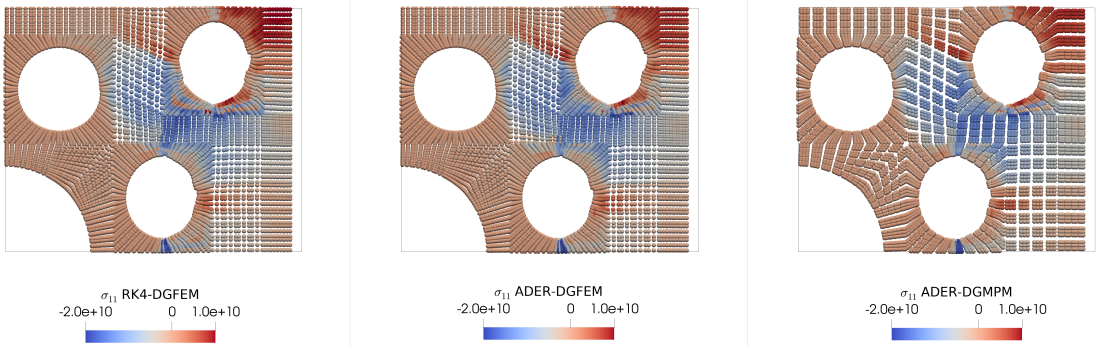

(b) $t \approx 3.63 \cdot 10^{-6}$ seconds.

Figure 12: Maps of the Cauchy stress component σ_{11} plotted in the current configuration of the multi-holed elementary cell at various times, computed with RK4-DGFEM, ADER-DGFEM and ADER-DGMPM. Results are obtained with a bi-quadratic polynomial order in space (S2), and quadratic one in time (T2) for ADER schemes. Maps are made with pointwise extraction of fields either at Gauss-Legendre interpolation points (for RK4-DGFEM and ADER-DGFEM), or at material points (ADER-DGMPM).

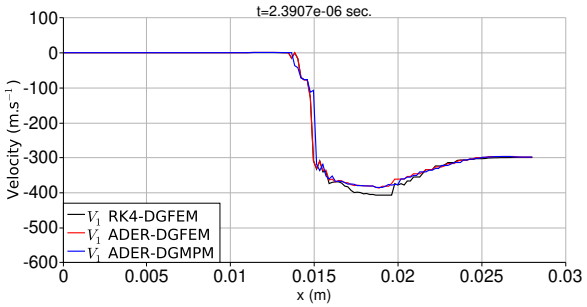

(a) $t \approx 2.39 \cdot 10^{-6}$ seconds.

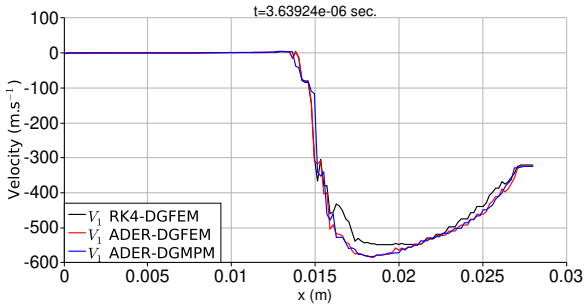

(b) $t \approx 3.63 \cdot 10^{-6}$ seconds.

Figure 13: Plots of the velocity component V_1 along the bottom line of the multi-holed medium at various times, computed with RK4-DGFEM, ADER-DGFEM and ADER-DGMPM. Results are obtained with a bi-quadratic polynomial order in space (S2), and a quadratic one in time (T2) for ADER schemes.

of the various numerical methods compared here, notice also that the limiter used (see Section 3.3) may also have an influence on the results, especially as strains become important. In particular the approximate solutions in the two ligaments lying between the right holes and the top and bottom lines of the computational domain may become sensitive to small variations as strains increases. As already pointed out in [46], this basic limiting algorithm has been

developed for scalar variables, and is thus not frame invariant and may lead to rotational symmetry distortion. The construction of a Lagrangian frame invariant limiter compatible with System (5), in the spirit of [44, 58], may then help to preserve rotational symmetries, and simulate higher strain levels before discarding the arbitrary computational grid.

6. Conclusion

The first-order accurate DGMPM has been extended in this work to arbitrary high orders of approximation. The considered applications pertain to hyperbolic problems defined in solid media submitted to impacts and undergoing large strains. The proposed extension of the DGMPM relies on the ADER technology. The latter here appears as a particular discrete time integrator well-suited to ensure the compatibility between constitutive updates set only at material points and discrete time advancement performed on a computational grid, while RK-type time integrators would require more remapping steps of various fields. More precisely, the ADER technology when applied to DGMPM was adapted on two items with respect to that applied to DGFEM: (i) the degrees of freedom of the space-time approximation of the predictor are now defined at materials points (at each intermediate times), and not at Gauss-Legendre interpolation points anymore, (ii) the spatial contribution to the space-time approximation of the predictor is now provided by a Moving Least Square Approximation (and not by a tensor product of one-dimensional Lagrange polynomials anymore). MLS permits on the one hand to reconstruct a smooth approximation of arbitrary order from scattered data, and on the other hand to perform the forward projection from material points to the degrees of freedom of the grid at the same time than the predictor approximation is being computed. The solution of the predictor approximation over the space-time slab $\Omega_e \times [t_n, t_{n+1}]$, and the DGFEM correction step then basically follow the same lines than those of ADER-DGFEM. Once a slope limiter has been applied to the updated field defined on the computational grid, a back-mapping permits to get the fields at material points via a PIC or a FLIP procedure, followed by a last constitutive update performed at these material points. Then, if required, the grid can be discarded for any adaption purpose. Notice that thanks to the total Lagrangian framework, the approximations related to the grid and to the predictor are computed once and for all, until the grid is discarded. Finally, some illustrations on examples of two-dimensional Lagrangian isothermal hyperelastodynamics have shown a good agreement between numerical solutions computed with RK-DGFEM, ADER-DGFEM and ADER-DGMPM.

Data availability statement

Data are available on request from the authors.

References

[1] Ayachit, U., 2015. The paraview guide: a parallel visualization application. Kitware, Inc.

[2] Bardenhagen, S.G., Kober, E.M., 2004. The generalized interpolation material point method. Computer Modeling in Engineering and Sciences 5, 477–496.

[3] Barradas, S., Jeandin, M., Bolis, C., Berthe, L., Arrigoni, M., Boustie, M., Barbezat, G., 2004. Study of adhesion of PROTAL® copper coating of Al 2017 using the laser shock adhesion test (LASAT). Journal of materials science 39, 2707–2716.

[4] Barth, T., Jespersen, D., 1989. The design and application of upwind schemes on unstructured meshes, in: 27th Aerospace sciences meeting, p. 366.

[5] Barton, P., Drikakis, D., Romenskii, E., 2010. A high-order Eulerian Godunov method for elastic-plastic flow in solids. International Journal for Numerical Methods in Engineering 81, 453–484.

[6] Belytschko, T., Krongauz, Y., Organ, D., Fleming, M., Krysl, P., 1996. Meshless methods: An overview and recent developments. Computer Methods in Applied Mechanics and Engineering 139, 3–47.

[7] Belytschko, T., Liu, W., Moran, B., 2000. Nonlinear finite elements for continua and structures. Wiley.

[8] Ben-Artzi, M., Falcovitz, J., 1984. A second-order godunov-type scheme for compressible fluid dynamics. Journal of Computational Physics 55, 1–32.

[9] Bonet, J., Lee, C.H., Gil, A.J., Ghavamian, A., 2021. A first order hyperbolic framework for large strain computational solid dynamics. part iii: Thermo-elasticity. Computer Methods in Applied Mechanics and Engineering 373, 113505.

[10] Bonet, J., Wood, R.D., 1997. Nonlinear continuum mechanics for finite element analysis. Cambridge university press.

[11] Boscheri, W., Dumbser, M., 2013. Arbitrary-lagrangian-eulerian one-step weno finite volume schemes on unstructured triangular meshes. Communications in Computational Physics 14, 1174–1206.

[12] Boscheri, W., Dumbser, M., Loubère, R., Maire, P.H., 2018. A second-order cell-centered lagrangian ader-mood finite volume scheme on multidimensional unstructured meshes for hydrodynamics. Journal of Computational Physics 358, 103–129.

[13] Boscheri, W., Loubère, R., Maire, P.H., 2022. A 3d cell-centered ader mood finite volume method for solving updated lagrangian hyperelasticity on unstructured grids. Journal of Computational Physics 449, 110779.
[14] Brackbill, J.U., Kothe, D.B., Ruppel, H.M., 1988. Flip: a low-dissipation, particle-in-cell method for fluid flow. Computer Physics Communications 48, 25–38.
[15] Busto, S., Chiocchetti, S., Dumbser, M., Gaburro, E., Peshkov, I., 2020. High order ader schemes for continuum mechanics. Frontiers in Physics 8, 32.
[16] Camacho, G., Ortiz, M., 1997. Adaptive lagrangian modelling of ballistic penetration of metallic targets. Computer methods in applied mechanics and engineering 142, 269–301.
[17] Cockburn, B., Shu, C.W., 2001. Runge–kutta discontinuous galerkin methods for convection-dominated problems. Journal of Scientific Computing 16, 173–261.
[18] Crutzen, Y., Boman, R., Papeleux, L., Ponthot, J.P., 2016. Lagrangian and arbitrary lagrangian eulerian simulations of complex roll-forming processes. Comptes Rendus Mecanique 344, 251–266.
[19] Dumbser, M., Balsara, D.S., Toro, E.F., Munz, C.D., 2008a. A unified framework for the construction of one-step finite volume and discontinuous galerkin schemes on unstructured meshes. Journal of Computational Physics 227, 8209–8253.
[20] Dumbser, M., Enaux, C., Toro, E.F., 2008b. Finite volume schemes of very high order of accuracy for stiff hyperbolic balance laws. Journal of Computational Physics 227, 3971–4001.
[21] Dumbser, M., Loubère, R., 2016. A simple robust and accurate a posteriori sub-cell finite volume limiter for the discontinuous galerkin method on unstructured meshes. Journal of Computational Physics 319, 163–199.
[22] Gassner, G., Dumbser, M., Hindenlang, F., Munz, C.D., 2011. Explicit one-step time discretizations for discontinuous galerkin and finite volume schemes based on local predictors. Journal of Computational Physics 230, 4232–4247.
[23] Gavrilyuk, S., Ndanou, S., Hank, S., 2016. An example of a one-parameter family of rank-one convex stored energies for isotropic compressible solids. Journal of Elasticity 124, 133–141.
[24] Ghavamian, A., Lee, C.H., Gil, A.J., Bonet, J., Heuzé, T., Stainier, L., 2021. An entropy-stable smooth particle hydrodynamics algorithm for large strain thermo-elasticity. Computer Methods in Applied Mechanics and Engineering 379, 113736.
[25] Gil, A.J., Lee, C.H., Bonet, J., Ortigosa, R., 2016. A first order hyperbolic framework for large strain computational solid dynamics. part ii: Total lagrangian compressible, nearly incompressible and truly incompressible elasticity. Computer Methods in Applied Mechanics and Engineering 300, 146–181.
[26] Godunov, S.K., 1959. Finite difference method for numerical computation of discontinuous solutions of the equations of fluid dynamics. Mathematicheskii Sbornik 47(89), 271–306.
[27] Gong, M., 2015. Improving the Material Point Method. Ph.D. thesis. University of New Mexico.
[28] H. Harlow, F., 1962. The particle-in-cell method for numerical solution of problems in fluid dynamics. Proc. Symp. Appl. Math. 15. doi:10.1090/psapm/015/9942.
[29] Hammerquist, C.C., Nairn, J.A., 2017. A new method for material point method particle updates that reduces noise and enhances stability. Computer methods in applied mechanics and engineering 318, 724–738.
[30] Harten, A., 1997. High resolution schemes for hyperbolic conservation laws. Journal of computational physics 135, 260–278.
[31] Harten, A., Engquist, B., Osher, S., Chakravarthy, S., 1987. Uniformly high order accurate essentially non-oscillatory schemes iii. Journal of Computational Physics 71, 231–303.
[32] Harten, A., Osher, S., 1987. Uniformly high-order accurate nonoscillatory schemes i. SIAM J. Num. Anal. 24, 279–309.
[33] Heuzé, T., Stainier, L., 2022. A variational formulation of thermomechanical constitutive update for hyperbolic conservation laws. Computer Methods in Applied Mechanics and Engineering 394, 114893.
[34] Hidalgo, A., Dumbser, M., 2011. Ader schemes for nonlinear systems of stiff advection–diffusion–reaction equations. Journal of Scientific Computing 48, 173–189.
[35] Hill, D., Pullin, D., Ortiz, M., Meiron, D., 2010. An Eulerian hybrid WENO centered-difference solver for elastic-plastic solids. Journal of Computational Physics 229, 9053–9072.
[36] Jackson, H., 2017. On the eigenvalues of the ader-weno galerkin predictor. Journal of Computational Physics 333, 409–413.
[37] Lancaster, P., Salkauskas, K., 1981. Surfaces generated by moving least squares methods. Mathematics of computation 37, 141–158.
[38] Lee, C.H., Gil, A.J., Bonet, J., 2013. Development of a cell centred upwind finite volume algorithm for a new conservation law formulation in structural dynamics. Computers & Structures 118, 13–38.
[39] Lee, C.H., Gil, A.J., Ghavamian, A., Bonet, J., 2019. A total lagrangian upwind smooth particle hydrodynamics algorithm for large strain explicit solid dynamics. Computer Methods in Applied Mechanics and Engineering 344, 209–250.
[40] Leveque, R., 2002. Finite volume methods for hyperbolic problems. Cambridge University Press.
[41] Leveque, R.J., 1997. Wave propagation algorithms for multidimensional hyperbolic systems. Journal of Computational physics 131, 327–353.
[42] Li, S., Liu, W.K., 2002. Meshfree and particle methods and their applications. Appl. Mech. Rev. 55, 1–34.
[43] Lucy, L.B., 1977. A numerical approach to the testing of the fission hypothesis. The astronomical journal 82, 1013–1024.
[44] Luttwak, G., Falcovitz, J., 2011. Slope limiting for vectors: A novel vector limiting algorithm. International Journal for Numerical Methods in Fluids 65, 1365–1375.
[45] Ma, S., Zhang, X., Qiu, X., 2009. Comparison study of mpm and sph in modeling hypervelocity impact problems. International journal of impact engineering 36, 272–282.
[46] Maire, P.H., 2011. A high-order one-step sub-cell force-based discretization for cell-centered lagrangian hydrodynamics on polygonal grids. Computers & Fluids 46, 341–347.
[47] Marusich, T., Ortiz, M., 1995. Modelling and simulation of high-speed machining. International Journal for Numerical Methods in Engineering 38, 3675–3694.
[48] Miller, G., Collela, P., 2001. A high-order eulerian godunov method for elastic-plastic flow in solids. Journal of Computational Physics 167, 131–176.
[49] Monaghan, J.J., 1992. Smoothed particle hydrodynamics. Annual review of astronomy and astrophysics 30, 543–574.

[50] Nayroles, B., Touzot, G., Villon, P., 1992. Generalizing the finite element method: diffuse approximation and diffuse elements. Computational mechanics 10, 307–318.
[51] Ndanou, S., Favrie, N., Gavrilyuk, S., 2015. Multi-solid and multi-fluid diffuse interface model: Applications to dynamic fracture and fragmentation. Journal of Computational Physics 295, 523–555.
[52] Nguyen, V.P., Rabczuk, T., Bordas, S., Duflot, M., 2008. Meshless methods: A review and computer implementation aspects. Mathematics and Computers in Simulation 79, 763–813.
[53] Plohr, B.J., Sharp, D.H., 1988. A conservative eulerian formulation of the equations for elastic flow. Advances in Applied Mathematics 9, 481 – 499.
[54] Qiu, J., Dumbser, M., Shu, C.W., 2005. The discontinuous galerkin method with lax–wendroff type time discretizations. Computer methods in applied mechanics and engineering 194, 4528–4543.
[55] Renaud, A., Heuzé, T., Stainier, L., 2018. A discontinuous galerkin material point method for the solution of impact problems in solid dynamics. Journal of computational physics 369, 80–102.
[56] Renaud, A., Heuzé, T., Stainier, L., 2020a. The discontinuous galerkin material point method for variational hyperelastic–plastic solids. Computer Methods in Applied Mechanics and Engineering 365, 112987.
[57] Renaud, A., Heuzé, T., Stainier, L., 2020b. Stability properties of the discontinuous galerkin material point method for hyperbolic problems in one and two space dimensions. International Journal for Numerical Methods in Engineering 121, 664–689.
[58] Sambasivan, S.K., Shashkov, M.J., Burton, D.E., 2013. Exploration of new limiter schemes for stress tensors in lagrangian and ale hydrocodes. Computers & Fluids 83, 98–114.
[59] Schwartzkopff, T., Munz, C.D., Toro, E.F., 2002. Ader: A high-order approach for linear hyperbolic systems in 2d. Journal of Scientific Computing 17, 231–240.
[60] Shepard, D., 1968. A two-dimensional interpolation function for irregularly-spaced data, in: Proceedings of the 1968 23rd ACM national conference, pp. 517–524.
[61] Shu, C.W., 2020. Essentially non-oscillatory and weighted essentially non-oscillatory schemes. Acta Numerica 29, 701–762.
[62] Sulsky, D., Chen, Z., Schreyer, H.L., 1994. A particle method for history-dependent materials. Computer methods in applied mechanics and engineering 118, 179–196.
[63] Sweby, P., 1984. High resolution schemes using flux limiters for hyperbolic conservation laws. SIAM Journal on Numerical Analysis 21, 995–1011.
[64] Tavelli, M., Chiocchetti, S., Romenski, E., Gabriel, A.A., Dumbser, M., 2020. Space-time adaptive ader discontinuous galerkin schemes for nonlinear hyperelasticity with material failure. Journal of computational physics 422, 109758.
[65] Titarev, V.A., Toro, E.F., 2002. Ader: Arbitrary high order godunov approach. Journal of Scientific Computing 17, 609–618.
[66] Toro, E., 2013. Riemann solvers and numerical methods for fluid dynamics. Springer.
[67] Toro, E.F., Millington, R., Nejad, L., 2001. Towards very high order godunov schemes, in: Godunov methods: theory and applications, Springer. pp. 907–940.
[68] Trangenstein, J., Collela, P., 1991. A higher-order Godunov method for modeling finite deformation in elastic-plastic solids. Communications in Pure Applied mathematics 47, 41–100.
[69] Van Leer, B., 1979. Towards the ultimate conservative difference scheme. v. a second-order sequel to godunov's method. Journal of Computational Physics 32, 101–136.
[70] Venkatakrishnan, V., 1995. Convergence to steady state solutions of the euler equations on unstructured grids with limiters. Journal of computational physics 118, 120–130.